TITLE: Impairment of the glial phagolysosomal system drives prion-like propagation in a *Drosophila* model of Huntington's disease

ABBREVIATED TITLE: Glial phagocytic defects drive huntingtin toxicity

AUTHORS and AFFILIATIONS: Graham H. Davis[1,2], Aprem Zaya[2], and Margaret M. Panning Pearce[1,2,*]

[1]Saint Joseph's University, Department of Biology, Philadelphia, PA 19131 and [2]University of the Sciences, Department of Biological Sciences, Philadelphia, PA 19104

*Corresponding author: Maggie Panning Pearce, mpearce@sju.edu

Number of pages: 41

Number of figures and tables: 7 main figures, 8 supplemental figures, 4 supplemental tables

Number of words in Abstract: 250

Number of words in Introduction: 607

Number of words in Discussion: 1357

CONFLICT OF INTEREST STATEMENT: The authors declare no conflicts of interest.

ACKNOWLEDGMENTS: We would like to thank David S. Tomlinson, Sabrina Abbruzzese, and Georgiana Moore for their assistance in collecting and imaging samples. Thank you to all former and current members of the Pearce Lab for their support in bringing this work to fruition. This work was funded by grants from the NIH (NS128847) and W.W. Smith Charitable Trusts.

ABSTRACT

Amyloid aggregate accumulation and spread between synaptically-connected regions of the brain is a hallmark of neurodegenerative disease progression. Glia participate in neuropathogenesis by reducing protein aggregate loads via phagocytosis while simultaneously acting as vectors for aggregate spread between cells. Emerging evidence supports the hypothesis that aggregate accumulation compromises the ability of glia to clear toxic material from the brain, possibly by disrupting the phagolysosomal compartment. A better understanding of how glia become deficient in the disease state could reveal novel therapeutic targets. Here, we report that mutant huntingtin (mHTT) aggregates impair glial responsiveness to injury and capacity to degrade axonal debris in a *Drosophila* model of Huntington's disease (HD). mHTT aggregate formation in neurons slowed engulfment and clearance of injured axons and caused accumulation of late phagosomes and lysosomes in glia. Neuronal mHTT expression induced innate immunity and phagocytic genes, some of which regulated mHTT aggregate burden in the brain. A forward genetic screen targeting glial Rab GTPases revealed Rab10 as a novel modifier of mHTT aggregate transmission from neurons to glia that acts downstream of the phagocytic receptor, Draper. This suggests that Rab-mediated intercellular vesicle sorting mechanisms could create opportunities for prion-like mHTT aggregates to escape lysosomal degradation. Together, our findings support a model in which mHTT aggregate build-up within the phagolysosomal system impairs glial phagocytosis while also promoting the generation of seeding-competent pathological proteins. The new mechanistic information we report here adds to a growing recognition of phagocytic glia as double-edged players in prion-like proteopathies such as HD.

SIGNIFICANCE STATEMENT

Deposition of amyloid aggregates is closely associated with neurodegenerative disease progression and neuronal death. Recent studies highlight glia as dynamic mediators of disease, capable of phagocytosing dying neurons and amyloid aggregates, while also inducing chronic inflammation and promoting proteopathic spread. Thus, glia have emerged as promising therapeutic targets for disease intervention. Here, we demonstrate in a *Drosophila* model of Huntington's disease that neuronal mHTT aggregates interfere with glial phagocytic functions, stimulate innate immunity signaling, and impair phagolysosomal processing. We also identify Rab10 as a novel modifier of prion-like transmission of mHTT aggregates, suggesting that Rab-mediated intramembrane fusion in the phagolysosomal system could drive aggregate pathology spread.

INTRODUCTION

Neuron-glia crosstalk is critical for maintaining homeostasis in the central nervous system (CNS), and disruption of these intercellular interactions is increasingly recognized as a central component of many neurological disorders, including neurodegenerative diseases. Glia perform immune surveillance functions in the CNS and respond to neuronal injury by altering gene expression (Magaki et al., 2018) and clearing damaged cells (Raiders et al., 2021; Zheng and Tuszynski, 2023). These glial responses may initially be neuroprotective, but prolonged glial reactivity propels the neurodegenerative disease state, for example, by driving premature loss of living neurons or functional synapses (Neniskyte et al., 2011; Hong et al., 2016; Dejanovic et al., 2022) and inducing neuroinflammation (Liddelow et al., 2017). Expanding our understanding of how glia influence neuron function and survival may contribute to the development of new therapeutic strategies potentially targeting non-neuronal cells.

A pathological hallmark of most neurodegenerative diseases is accumulation of misfolded proteins into intra- or extracellular amyloid aggregates in vulnerable brain regions (Knowles et al., 2014). Protein aggregates arise due to age-associated decline in cellular protein folding capacity (Santra et al., 2019; Stein et al., 2022) and overwhelmed degradative pathways, including the ubiquitin-proteasome system, autophagy, and phagocytosis (Aman et al., 2021; Duong et al., 2021; Wodrich et al., 2022). As professional phagocytes of the brain, microglia and astrocytes clear damaged and dysfunctional cells (Paolicelli et al., 2011; Wakida et al., 2018; Herzog et al., 2019; Lee et al., 2021) and other pathogenic material such as protein aggregates (Liu et al., 2017; Choi et al., 2020). Defective glial clearance of debris may be a driving force underlying neurodegenerative disease, highlighted by a growing list of genetic risk variants associated with phagocytic and endolysosomal pathways (Podleśny-Drabiniok et al., 2020). Endolysosomal impairment promotes protein aggregate accumulation; in turn, these aggregates can drive further endolysosomal dysfunction, including deacidification and membrane permeabilization (Krasemann et al., 2017; Heckmann et al., 2019; Burbidge et al., 2022; Lee et al., 2022). Incompletely degraded aggregates may acquire the ability to spread and seed soluble proteins in a prion-like manner in the brain (Jucker and Walker, 2018; Monaco and Fraldi, 2020).

Mechanisms by which pathogenic aggregates dysregulate lysosomal degradation pathways remain largely unknown. Intracellular membrane fusion events that underlie endo/phagosome maturation are catalyzed by Rab GTPases (Ng and Tang, 2008; Chan et al., 2011; Langemeyer et al., 2018), which cycle

between active (GTP-bound) and inactive (GDP-bound) states to organize endomembranes into distinct functional domains (Hall, 1990; Chan et al., 2011). Rab dysfunction is implicated in neurodegenerative diseases—e.g., increased expression of Rab4, Rab5, Rab7, and Rab27 has been observed in Alzheimer's disease (AD) (Ginsberg et al., 2011), and several Rabs are known substrates of leucine rich repeat kinase 2 (LRRK2), a genetic risk factor in familial Parkinson's disease (PD) (Jeong et al., 2018). Intriguingly, spreading of α-synuclein between cultured neuronal and enteroendocrine cells is mediated by the LRRK2 substrate Rab35 (Bae et al., 2018; Rodrigues et al., 2022), suggesting that Rab-dependent processes may contribute to formation and propagation of prion-like aggregate seeds.

Here, we examined how protein aggregates generated in neurons affect phagocytic glial functions in a *Drosophila* model of Huntington's disease (HD). We report that neuronal expression of aggregation-prone mutant huntingtin (mHTT) reduces the ability of glia to clear axonal debris and mount transcriptional responses involving phagocytosis and innate immune signaling genes following acute nerve injury. We also observed mHTT-induced changes to lysosomes and Rab+ vesicles in uninjured brains, and identify Rab10 as a novel modifier of prion-like spreading of mHTT aggregates in adult fly brains. Together, these studies shed light on mechanisms by which phagocytic glia respond to and are impaired by accumulation of pathogenic aggregates in neurons.

95 **MATERIALS AND METHODS**

96 *Fly Husbandry*

97 Fly stocks and crosses were raised on standard cornmeal/molasses media on a 12 hr light/12 hr dark
98 cycle at 25°C, unless otherwise noted. Transgenic or mutant flies were either generated by our lab, purchased
99 from Bloomington Drosophila Stock Center, or kindly provided by collaborators as indicated in Table S1.
00 Genotypes and sources of all fly stocks used in this study are listed in Table S1.

01

02 *Cloning and Microinjection*

03 pQUASTattB(HTT$_{ex1}$Q25-V5) and pQUASTattB(HTT$_{ex1}$Q91-V5) plasmids were cloned by PCR
04 amplification of HTT$_{ex1}$ cDNAs using a reverse primer that inserted an in-frame, C-terminal V5 tag
05 (GKPIPNPLLGLDST) and ligation into the pQUASTattB vector backbone via XhoI and XbaI restriction sites.
06 pUASTattB(pHluorin-HTT$_{ex1}$Q25-tdTomato) and pUASTattB(pHluorin-HTT$_{ex1}$Q91-tdTomato) plasmids were
07 generated by PCR amplification of HTT$_{ex1}$ cDNAs and subcloning to replace the CD4 sequence in the
08 pUASTattB(MApHS) plasmid (Han et al., 2014) via In-Fusion cloning (Takara Bio USA, Inc. Mountain View,
09 CA). These plasmids were microinjected into embryos with the attP24, VK19, or VK27 φC31 attP integration
10 sites at BestGene, Inc (Chino Hills, CA). See Table S1 for detailed genotype information for these transgenic
11 flies.

12

13 *Drosophila brain dissection and sample preparation*

14 Adult fly brains were dissected in ice-cold phosphate-buffered saline (PBS) containing either no
15 detergent or 0.03% (PBS/0.03T), 0.1% (PBS/0.1T), or 0.3% (PBS/0.3T) Triton X-100. Dissected brains were
16 fixed in 4% paraformaldehyde (PFA) in the dark at room temperature (RT) for 20 minutes. For imaging GFP
17 and mCherry fluorescence, brains were washed 7X in PBS/0.03T buffer before incubation in Slowfade Gold
18 Antifade Mountant (Invitrogen, Carlsbad, CA). When imaging pHluorin-tagged and other pH-sensitive
19 constructs, such as GFP-LAMP1, brains were washed 7X in PBS for at least 50 minutes at RT before
20 incubation in Slowfade. For immunostaining, brains were washed 7X in PBS/0.3T after fixation, blocked in
21 PBS/0.3T containing 5% normal goat serum (Lampire Biological Laboratories, Pipersville, PA) for 30 min at
22 RT, incubated in primary antibodies diluted in blocking solution for 24-48 hours at 4°C, washed 7X in

23 PBS/0.3T, and then incubated in secondary antibodies diluted in blocking solution for 16-20 hours at 4°C. After
24 a final set of 7X PBS/0.3T washes, the brains were incubated in Slowfade. For Magic Red and LysoTracker
25 staining, brains were dissected in PBS and incubated in 1:1000 LysoTracker Red DND-99 (Invitrogen,
26 Carlsbad, CA) or 1:1250 Magic Red (ImmunoChemistry, Davis, CA) diluted in PBS for 20 minutes at RT.
27 Brains were washed 5X in PBS for 15 min total, fixed in 4% PFA in PBS/0.1T for 20 minutes at RT, washed 6X
28 in PBS/0.1T for 30 min total, and incubated in Slowfade. Following incubation in Slowfade for 1-24 hours at
29 4°C in the dark, all brains were bridge-mounted in Slowfade on glass microscopy slides under #1.5 coverglass,
30 and edges were sealed using clear nail polish.

31 Primary antibodies used in this study include: chicken anti-GFP (RRID: AB_300798; 1:1000; Abcam,
32 Cambridge, UK), rat anti-N-cadherin (clone DN-Ex #8; RRID: AB_528121; 1:75; Developmental Studies
33 Hybridoma Bank, Iowa City, IA), mouse anti-Repo (8D12 Repo; RRID: AB_528448; 1:25; Developmental
34 Studies Hybridoma Bank, Iowa City, IA), mouse anti-V5 (RRID: AB_2556564; 1:125; Thermo Fisher Scientific
35 Inc., Waltham, MA), and rabbit anti-Draper (1:500; a kind gift from Marc Freeman, Vollum Institute, Portland,
36 OR). Secondary antibodies include FITC-conjugated donkey anti-chicken (RRID: AB_2340356; 1:250; Jackson
37 Immuno Research Labs, West Grove, PA), AlexaFluor 568 goat anti-mouse (RRID: AB_2534072; 1:250),
38 AlexaFluor 647 goat anti-rabbit (RRID: AB_2535812; 1:250) and AlexaFluor 647 goat anti-rat IgGs (RRID:
39 AB_141778; 1:250) (Invitrogen, Carlsbad, CA).
40

41 *Image Acquisition*

42 All microscopy data were collected on a Leica SP8 laser-scanning confocal system equipped with 405
43 nm, 488 nm, 561 nm, and 633 nm lasers and 40X 1.3 NA or 63X 1.4 NA oil objective lenses. Leica LAS-X
44 software was used to establish optimal settings during each microscopy session and to collect optical z-slices
45 of whole-mounted brain samples with Nyquist-optimized sampling criteria. Optical zoom was used to magnify
46 and establish regions of interest (ROI) in each sample. For images showing a single glomerulus, confocal
47 slices were collected to generate ~73 x 73 x 20 μm (*xyz*) stacks, with z-axis boundaries established using
48 fluorescent signal in DA1 or VA1lm ORN axons. For images of a single antennal lobe, confocal slices were

collected to generate ~117 x 117 x 26 µm (*xyz*) stacks, which were located using HTT_{ex1} fluorescence in ORN axons.

Confocal image analyses

Raw confocal data were analyzed in 2D using ImageJ/FIJI (RRID:SCR_002285; NIH, Bethesda, MD) or in 3D using Imaris image processing software (RRID:SCR_007370; Bitplane, Zürich, Switzerland). Methods used for semi-automated quantification of ORN axons and mHTT or mHTT-seeded wtHTT aggregate numbers were previously described (Donnelly et al., 2020). Briefly, raw confocal data were cropped to establish an ROI for further analysis and displayed as a 2D sum intensity projection (ImageJ) or a 3D volume (Imaris). In **Figure 1**, mCD8-GFP and HTT-mCherry fluorescence was segmented using the 'Surfaces' function in Imaris, with surface detail set to 0.25µm and background subtraction at 0.75µm. Using the 'split touching objects' option, seed point diameter was set to 0.85µm. In **Figure 2**, pHluorin- and tdTomato-labeled VA1lm ORN axons were quantified in central 30x30 pixels, 50 slices ROIs from sum intensity projections of each VA1lm glomerulus. Background fluorescence was subtracted from raw confocal images. In **Figure 2**, pHluorin- and tdTomato-labeled Or83b+ ORN axons or MBN soma were quantified from central 100x100 pixels, 75 slices ROIs of each antennal lobe or mushroom body calyx, and background intensity was subtracted from sum intensity projections. In **Figure 3**, quantification of $Toll6^{MIMICGFP}$ fluorescence was performed using the 'Spots' function in Imaris (*xy* diameter set to 0.5µm and *z*-diameter of 1.0µm). Quantification of repo-associated GFP-Jra was performed using the "Surfaces" functions in Imaris to identify repo+ surfaces (surface detail = 0.2µm, background subtraction = 1.6µm, number of voxels >10).

In **Figures 4-7**, mHTT surfaces were quantified as previously reported (Donnelly et al., 2020). Briefly, mCherry+ surfaces were generated in Imaris (surface detail = 0.2µm, background subtraction = 0.45µm, and seed point diameter = 0.85µm). In **Figure S5-2**, $wtHTT_{ex1}$ surfaces were generated in Imaris (surface detail = 0.2µm, background subtraction = 0.45µm, and seed point diameter = 0.85µm). In **Figure 5 and S5-1**, MR+, LTR+, LAMP1-GFP or GFP-LAMP1 surfaces were generated in Imaris using the 'Surfaces' algorithm (surface detail = 0.2µm, background subtraction = 0.4µm). Surfaces were further filtered by volume (>0.001μm^3). In **Figures 5 and 7** and **supplemental figures for 5 and 7**, GFP-LAMP1+, YFP-Rab+, YRab+, MR+, or LTR+ surfaces overlapping HTT_{ex1}-V5, -GFP, or -mCherry signal were identified using the 'shortest distance' filter

77 (≤0.2 μm). We provide examples of this in **Fig S5-3** with GFP-LAMP1+ surfaces. In **Figure 7 and**
78 **supplemental figure S7**, YFP-Rab+ and YRab+ surfaces were segmented in Imaris using the 'Surfaces'
79 algorithm (surface detail = 0.2μm, background subtraction = 0.4μm, and surfaces were filtered by volume
80 >0.004μm^3).
81
82 *qPCR*
83 Transgenic *Drosophila* were flash frozen in liquid nitrogen, and heads were collected using a
84 microsieve with a 230 nm filter to separate bodies from heads and 170 nm filter to separate heads from
85 appendages. Total RNA was extracted from isolated fly heads using the Zymo Direct-Zol RNA miniprep kit
86 (Zymo Research, Irvine, CA). Extracted RNA was quantified on a Nanodrop 2000 (Thermo Fisher Scientific),
87 and equal quantities of each sample were subjected to cDNA synthesis using the High-Capacity cDNA
88 Reverse Transcription Kit (Applied Biosystems, Waltham, MA). qPCR was performed on a Bio-rad T100
89 Thermal Cycler with a CFX384 Real-Time System (Bio-Rad Laboratories, Hercules, CA) using 10 ng of input
90 RNA per replicate, TB Green Premix Ex Taq II (Takara Bio, Kusatsu, Japan). All qPCR primers are listed in
91 Table S2.
92
93 *Experimental Design and Statistical Analyses*
94 All quantified data were organized and analyzed in Prism 9 software (Graphpad, San Diego, CA). We
95 performed power analyses to determine appropriate sample sizes for each experiment using a Sample Size
96 calculator available at ClinCalc.com ($\alpha = 0.05$, $\beta = 0.2$). All quantifications are graphed as mean ± s.e.m. Mean
97 values, statistical tests, and sample sizes (*n*) for each experiment are described in a table attached to each
98 figure. In general, a single glomerulus or antennal lobe represented one biological replicate. Statistical
99 comparisons were performed using the following tests where appropriate: unpaired, 2-tailed Student's *t*-test
00 when comparing two samples and one-way ANOVA followed by *post hoc* multiple comparison tests when
01 comparing ≥3 samples.
02

RESULTS

Expression of mHTT in neurons inhibits phagocytic clearance of axonal debris

HD is a monogenic neurodegenerative disease caused by expansion of a CAG repeat region in exon 1 of the *huntingtin* (*HTT/IT15)* gene beyond a pathogenic threshold of 37 repeats, leading to production of mHTT proteins containing expanded N-terminal polyglutamine (polyQ≥37) tracts (Scherzinger et al., 1999). mHTT proteins are prone to misfolding and accumulate into insoluble aggregates (Wanker, 2000), whereas wild-type HTT (wtHTT) proteins containing polyQ≤36 tracts remain soluble unless seeded by a pre-formed HTT aggregate (Preisinger et al., 1999; Chen et al., 2001). To recapitulate these molecular features of HD, we generated transgenic flies that express N-terminal exon 1 fragments of human mHTT ($mHTT_{ex1}$) containing a polyQ91 tract or wtHTT ($wtHTT_{ex1}$) with a polyQ25 tract via the GAL4-UAS (Brand and Perrimon, N., 1993) or QF-QUAS binary expression systems (Potter and Luo, 2011). As we have previously reported (Pearce et al., 2015; Donnelly et al., 2020), fluorescent protein fusions of $mHTT_{ex1}$ and $wtHTT_{ex1}$ appeared punctate (i.e., aggregated or insoluble) or diffuse (i.e., soluble), respectively, in axon termini of the DA1 type of olfactory receptor neurons (ORNs), which synapse in the DA1 glomerulus of the antennal lobe in the central adult fly brain (Couto et al., 2005) (Fig. 1A-B). To determine if neuronal $mHTT_{ex1}$ expression affects the ability of glial cells to clear neuronal debris in the adult fly CNS, we co-expressed each mCherry-tagged HTT_{ex1} transgene with membrane-targeted GFP (mCD8-GFP) in DA1 ORNs and measured GFP and mCherry fluorescence intensities following acute injury to the antennal nerve (Fig. 1A-D). Surgical removal of the second and third antennal segments initiates Wallerian degeneration of ORN axons and leads to the clearance of most axonal debris in the central brain within 7 days (MacDonald et al., 2006) (Fig. 1C). Interestingly, $mHTT_{ex1}$ expression was associated with reduced steady-state mCD8-GFP levels in DA1 ORN axons in 2 and 4 week-old flies (Fig. S1A), likely due to neurotoxicity associated with $mHTT_{ex1}$ expression. However, quantification of DA1 ORN axons remaining after antennal nerve injury revealed that glial clearance of the axonal debris was reduced in flies co-expressing neuronal $mHTT_{ex1}$ compared with controls expressing $wtHTT_{ex1}$ (Fig. 1A-C). Further, this effect of $mHTT_{ex1}$ expression was exacerbated in older flies (14- and 28-days-old) (Fig. 1C). Quantification of mCherry fluorescence indicated that clearance of axonal $mHTT_{ex1}$ was also slowed compared to $wtHTT_{ex1}$ (Fig. 1D), suggesting that glia are deficient in degrading axonal debris and neuronal $mHTT_{ex1}$ aggregates.

30 We also tested whether formation of $mHTT_{ex1}$ aggregates in glial cells impacts ORN axonal debris
31 clearance following acute injury. Restricting expression of $mHTT_{ex1}$ to glia resulted in appearance of
32 heterogeneously-sized $mHTT_{ex1}$ aggregates throughout glia (Fig. S1C-D). Glial $mHTT_{ex1}$ aggregates also
33 slowed injury-induced clearance of mCD8-GFP-labeled axons compared with $wtHTT_{ex1}$-expressing controls
34 (Fig. 1G). Together, these findings indicate that $mHTT_{ex1}$ aggregates slow the kinetics with which glia clear
35 injured ORN axons, whether the aggregates are engulfed from neurons or already present in the glial
36 cytoplasm.
37
38 *Neuronal mHTT aggregates impair nascent phagosome formation*
39 Phagocytosis occurs via 4 major steps: (1) extension of phagocyte membranes toward extracellular
40 "find me" cues, (2) recognition of "eat me" signals by scavenger receptors, (3) cytoskeletal and plasma
41 membrane reorganization to surround and internalize extracellular material, and (4) maturation of nascent
42 phagosomes through sequential endomembrane fusions that culminate with the lysosome (Vieira et al., 2002).
43 We have previously reported that the conserved scavenger receptor, Draper/Ced-1/MEGF10 (MacDonald et
44 al., 2006; Evans et al., 2015; Iram et al., 2016), regulates engulfment, clearance, and intercellular spreading of
45 $mHTT_{ex1}$ aggregates originating in ORN axons (Pearce et al., 2015; Donnelly et al., 2020). To test whether
46 delayed clearance of injured axons containing $mHTT_{ex1}$ aggregates (Fig. 1) could result from defective Draper-
47 dependent engulfment, we co-expressed V5-tagged $mHTT_{ex1}$ or $wtHTT_{ex1}$ with the ratiometric membrane-
48 associated pH sensor (MApHS), consisting of the transmembrane domain of CD4 flanked by N-terminal ecliptic
49 pHluorin and C-terminal tdTomato (Han et al., 2014), in the VA1lm type of ORNs. Ecliptic pHluorin is brightest
50 at pH 7.5 and dims as pH drops, quenching at pH <6.0 (Miesenböck et al., 1998), whereas tdTomato
51 fluorescence is pH resistant. Thus, internalization of MApHS-labeled ORN axonal debris into a rapidly-acidified
52 nascent phagosome can be monitored by calculating pHluorin:tdTomato fluorescence intensity ratios (Han et
53 al., 2014). Indeed, pHluorin:tdTomato ratios in VA1lm axons decreased 14 and 25 hours post-axotomy (Fig.
54 2A-C), and this effect was lost when *draper* was deleted from glia using the tissue-specific CRISPR/Cas9-TriM
55 method (Fig. 2C and S2A-C) (Poe et al., 2019), demonstrating that this construct accurately reports nascent
56 phagosome acidification following engulfment. Notably, this injury-induced decrease in pHluorin:tdTomato ratio

57 was less pronounced in ORN axons expressing $mHTT_{ex1}$ compared with $wtHTT_{ex1}$-expressing controls (Fig. 2A-
58 C), suggesting that $mHTT_{ex1}$ aggregates impair nascent phagosome formation during engulfment.
59
60 *Neuronal mHTT accumulates in low pH intracellular compartments*
61 We observed that $mHTT_{ex1}$ expression was associated with a slight but significant decrease in steady-
62 state pHluorin:tdTomato ratios in MApHS-labeled axons compared with $wtHTT_{ex1}$-expressing controls (Fig.
63 2D), suggesting that even in the absence of acute injury, $mHTT_{ex1}$ signals for ORN axon engulfment. To test
64 whether $mHTT_{ex1}$ itself accumulates in low pH cellular compartments, we generated transgenic flies that
65 express $mHTT_{ex1}$ or $wtHTT_{ex1}$ fused to N-terminal pHluorin and C-terminal tdTomato fluorescent proteins,
66 herein referred to as HTT-associated pH sensor, or "HApHS" (Fig. 2E-F). wtHApHS and mHApHS transgenes
67 were expressed in either Or83b+ ORNs, which encompass 70-80% of all adult ORNs (Larsson et al., 2004), or
68 mushroom body neurons (MBNs), which are downstream in the fly olfactory circuit and innervate the learning
69 and memory center of the fly CNS (McGuire et al., 2001). In both neuronal cell types, pHluorin:tdTomato ratios
70 associated with mHApHS expression were significantly decreased compared to wtHApHS (Fig. S2A-F),
71 suggesting that $mHTT_{ex1}$ proteins accumulate in acidified cellular compartments. To discriminate $mHTT_{ex1}$
72 proteins engulfed by glia from those sequestered in neuronal autophagolysosomes, we measured mHApHS
73 pHluorin:tdTomato ratios in VA1lm ORN axons after glial *draper* loss-of-function was achieved by CRISPR-
74 TRiM. Draper knockout increased pHluorin:tdTomato ratios of mHApHS (Fig. 2E-G), suggesting that at least
75 some portion of mHTT aggregates accumulate in the glial phagolysosomal system.
76
77 *Neuronal mHTT impairs injury-responsive gene upregulation*
78 Glia alter expression of many genes to elicit cellular responses to insult or injury in the brain. For
79 example, acute CNS injury in *Drosophila* increases transcription of many genes involved in phagocytosis and
80 innate immune signaling (Fig. 3B) (Purice et al., 2017; Byrns et al., 2021; Alphen et al., 2022). To test whether
81 the reduced ability of glia to engulf and clear $mHTT_{ex1}$ -containing axonal debris correlates with reduced injury
82 responsiveness, we used qPCR and GFP-tagged constructs of Toll-like receptor Toll-6 and the AP-1
83 transcription factor subunit Jra to quantify gene expression changes following $mHTT_{ex1}$ accumulation in axons
84 and/or acute axotomy. $mHTT_{ex1}$ expression in uninjured Or83b+ ORNs increased *drpr-I*, *toll-6,* and *relish*

transcripts between 1.2- and 1.5-fold (Fig. 3A) and levels of GFP-tagged Toll-6 and Jra proteins in the CNS (Fig. 3C-H), suggesting that neuronal $mHTT_{ex1}$ aggregates activate a mild injury response in the brain. Jra-GFP expression increased throughout the CNS and in Repo+ nuclei (Fig. 3H), suggesting that $mHTT_{ex1}$-induced upregulation of AP-1 can be at least partially attributed to glia. Following antennal and maxillary palp axotomy, *drpr-I* and *toll-6* upregulation was comparable to $mHTT_{ex1}$ expression alone, whereas other stress response genes (e.g., *dorsal, mmp1, relish,* and *ets21c)* had a far greater response to acute injury (Fig. 3A). Strikingly, injury-induced upregulation of each of these genes was significantly reduced by $mHTT_{ex1}$ expression in Or83b+ ORNs (Fig. 3A). Together, these data suggest that neuronal $mHTT_{ex1}$ aggregates inhibit transcriptional responses to neural injury in the brain.

The data we report here as well as previously published work (Pearce et al., 2015; Ray et al., 2017) demonstrates that $mHTT_{ex1}$ and Aβ aggregates induce *drpr-I* upregulation and that *drpr* knockout causes these aggregates to accumulate, suggesting that glia regulate pathogenic aggregate loads by activating phagocytosis. We next tested for the involvement of other phagocytic and innate immunity genes in neuronal $mHTT_{ex1}$ aggregate turnover using RNAi-mediated gene silencing in ensheathing glia, a subpopulation of Draper+ glia that wrap processes around synaptic neuropil and mediate clearance of injured ORN axons (Doherty et al., 2009). Consistent with our previous findings in all *repo*+ glia (Pearce et al., 2015), ensheathing glia were vulnerable to prion-like conversion of glial $wtHTT_{ex1}$ proteins by neuronal $mHTT_{ex1}$ aggregates (Fig. S4A, C-D). Conversely, seeding of $wtHTT_{ex1}$ expressed in astrocytic glia, which lack detectable Draper expression in the adult fly brain (Doherty et al., 2009), was not observed (Fig. S4B-D). Interestingly, knockdown of ensheathing glial Toll-6, NijA, and Relish increased $mHTT_{ex1}$ aggregate numbers in DA1 ORN axons (Fig. 4A-B). Similarly, adult-specific, pan-glial knockdown of Ets21c, which was found to be required for development, also increased numbers of $mHTT_{ex1}$ aggregates in DA1 ORN axons (Fig. 4C-D). Thus, several ensheathing glial genes with known roles in phagocytic and innate immunity pathways regulate basal turnover of $mHTT_{ex1}$ aggregates in ORN axons.

Neuronal mHTT aggregates are associated with defects in multiple endolysosomal compartments

Our findings thus far indicate that neuronal $mHTT_{ex1}$ aggregates elicit mild injury responses in the brain and reduce the ability of phagocytic glia to respond transcriptionally and functionally to acute nerve injury. We

13 have previously postulated that prion-like spreading of $mHTT_{ex1}$ in the fly CNS could be facilitated by escape of
14 engulfed aggregates from the endolysosomal compartment of phagocytic glia (Pearce et al., 2015; Donnelly et
15 al., 2020). Therefore, we sought to determine whether neuronal $mHTT_{ex1}$ aggregates are associated with
16 defects in endolysosomal processing in non-injured brains. We first measured effects of neuronal $mHTT_{ex1}$
17 expression on the quantity, size, and function of lysosomes using dyes that label active cathepsins and low pH
18 cellular compartments. Expression of $mHTT_{ex1}$ in Or83b+ ORNs increased numbers of lysosomes labeled by
19 the active cathepsin dye, Magic Red (MR), and the low pH sensor, LysoTracker Red (LTR), compared with
20 control brains expressing $wtHTT_{ex1}$ (Fig. S5-1A-F). Additionally, numbers of MR+ and LTR+ lysosomes that co-
21 localized with $mHTT_{ex1}$ were greater than for $wtHTT_{ex1}$ (Fig. S5-1C and F). We next assessed the impact of
22 neuronal $mHTT_{ex1}$ specifically on glial lysosomes by driving expression of lysosomal-associated membrane
23 protein 1 (LAMP1) tagged at its cytosolic C-terminus with GFP (LAMP1-GFP) in all glia. Neuronal $mHTT_{ex1}$
24 expression increased the overall number of glial LAMP1-GFP+ lysosomes and the number of LAMP1-GFP+
25 lysosomes associated with HTT signal. Additionally, LAMP1-GFP+ lysosomes associated with $mHTT_{ex1}$ were
26 enlarged compared with all lysosomes (Fig 5A-E).

27 To examine whether neuronal $mHTT_{ex1}$ aggregates affect lysosome integrity, we alternatively
28 expressed in glia a transgene encoding LAMP1 fused at its N-terminus to GFP. This construct integrates into
29 the lysosomal membrane such that GFP is exposed to the lumen, and loss of GFP signal can thus be used to
30 monitor LAMP1+ lysosome activity (Pulipparacharuvil et al., 2005). Interestingly, the quantity and diameter of
31 GFP-LAMP1+ vesicles were significantly increased in brains expressing $mHTT_{ex1}$ in Or83b+ ORNs (Fig. 5F-J).
32 GFP-LAMP1+ surfaces also strongly associated with $mHTT_{ex1}$ aggregates compared to wtHTT controls (Fig.
33 5G). These data demonstrate that the abundance and size of glial lysosomes increase in brains expressing
34 $mHTT_{ex1}$ in neurons, and suggest that $mHTT_{ex1}$ aggregates cause non-cell autonomous lysosome dysfunction.
35 To test whether lysosome function affects seeding competency of $mHTT_{ex1}$ aggregates, we used RNAi to
36 individually knockdown proteins with known roles in lysosome acidification, including subunits of the vacuolar
37 ATPase (V-ATPase) (Fig. S5-2A-C). Knockdown of two V-ATPase subunits, Vha68-3 (Portela et al., 2018) and
38 rabconnectin-3A (Yan et al., 2009), and Spinster, a late-endosomal and lysosomal efflux permease (Rong et
39 al., 2011), increased seeding of glial $wtHTT_{ex1}$ by neuronal $mHTT_{ex1}$ aggregates (Fig. S5-2A-C). While
40 knockdown of Vha16-1, a V-ATPase subunit that regulates endolysosome membrane fusion (Finbow et al.,

41 1994; Dunlop et al., 1995), did not affect seeding, it did cause accumulation of $mHTT_{ex1}$ aggregates in DA1
42 axons (Fig. S5-2B). Together, these findings suggest that disruption of glial lysosome function could lead to the
43 formation of seeding-competent $mHTT_{ex1}$ aggregates.
44
45 *The GTPase Rab10 mediates prion-like transmission of mHTT aggregates*
46 Lysosome dysfunction could occur secondary to upstream defects in endo/phagosome maturation. Our
47 prior work supports a model in which a portion of $mHTT_{ex1}$ aggregates engulfed by glia evade degradation
48 during phagosome maturation and/or phagolysosome formation (Pearce et al., 2015; Donnelly et al., 2020). To
49 test this model, we used forward genetic screening to interrogate roles for Rab GTPases in escape of engulfed
50 neuronal $mHTT_{ex1}$ aggregates from the phagolysosomal system. The *Drosophila* genome encodes 31 Rab and
51 Rab-like proteins, all of which have mammalian orthologs, and many of these GTPases have been implicated
52 in vesicle and target membrane fusion in cells (Zhang et al., 2007). To determine whether any *Drosophila* Rabs
53 mediate escape of phagocytosed $mHTT_{ex1}$ aggregates and seeding of $wtHTT_{ex1}$ in the glial cytoplasm, we
54 individually knocked down each Rab in *repo*+ glia using RNAi. Glial-restricted silencing of 23 of the 31 Rabs
55 produced viable adults, and these flies were used to monitor effects of Rab knockdown on $mHTT_{ex1}$-induced
56 aggregation of $wtHTT_{ex1}$ in glia. Only two Rab RNAi lines, $Rab10^{RNAi}$ and $Rab23^{RNAi\#2}$, significantly altered
57 numbers of induced $wtHTT_{ex1}$ aggregates (Fig. 6A-C). Of note, 3 additional Rab23 RNAi lines had no
58 significant effects on numbers of $wtHTT_{ex1}$ aggregates, suggesting that $Rab23^{RNAi\#2}$ may cause off-target
59 effects. Strikingly, Rab10 depletion reduced numbers of seeded $wtHTT_{ex1}$ aggregates, phenocopying effects of
60 Draper knockdown (Fig. 6C) and suggesting that Draper and Rab10 function in the same pathway. We tested
61 for genetic interaction between *drpr* and *rab10* using loss-of-function alleles to examine effects on $mHTT_{ex1}$
62 aggregate transmission from presynaptic DA1 ORNs to postsynaptic projection neurons (PNs), a process
63 previously reported to require transport though Draper-expressing glia (Donnelly et al., 2020). *rab10* knockout
64 was incompatible with expression of $mHTT_{ex1}$ and $wtHTT_{ex1}$ transgenes; similarly, reduced viability of *rab10*
65 null animals has been previously reported (Kohrs et al., 2021). Thus, we tested for epistasis between *drpr* and
66 *rab10* in heterozygous and trans-heterozygous animals. While there were no significant changes in $mHTT_{ex1}$
67 aggregate numbers (Fig. 6D), significantly fewer $wtHTT_{ex1}$ aggregates formed in PNs of $rab10^{+/-}$ $drpr^{+/-}$
68 transheterozygotes than in the individual heterozygotes (Fig. 6E). This same effect was not observed in

69 *rab14*$^{+/-}$ *drpr*$^{+/-}$ transheterozygous animals (Fig. 6E), indicating that the epistatic relationship is specific to *drpr*
70 and *rab10*. Thus, Draper and Rab10 appear to function in the same pathway that regulates prion-like
71 transmission of phagocytosed $mHTT_{ex1}$ aggregates in the fly brain.
72
73 *Neuronal mHTT aggregates alter numbers of early and late glial phagosomes*
74 Our forward genetic screen indicates that at least one glial Rab GTPase, Rab10, regulates the seeding
75 capacity of neuronal $mHTT_{ex1}$ aggregates. Interestingly, Rab10 has been reported to regulate phagosome
76 maturation in mammalian cells (Cardoso et al., 2010; Seto et al., 2011; Lee et al., 2020; Wang et al., 2023),
77 and Rab10 expression and activity are altered in neurodegenerative diseases such as AD and PD (Eguchi et
78 al., 2018; Tavana et al., 2018; Yan et al., 2018). Because little is known about Rab10's role in glia, we sought
79 to characterize this GTPase alongside two additional Rabs with well-established roles in endocytic pathways,
80 Rab5 and Rab7, markers of early and late endo/phagosomes, respectively (Hutagalung and Novick, 2011).
81 Interestingly, we found that *rab10*, *rab5*, and *rab7* were all upregulated between ~1.4 and 2.4-fold following
82 acute antennal nerve injury, and $mHTT_{ex1}$ expression in Or83b+ ORNs caused upregulation of *rab10* and *rab7*
83 each by ~1.2-fold (Fig. S7-1A). Interestingly, injury-induced upregulation of *rab5* and *rab7* was inhibited by
84 ~50% and ~100%, respectively, in flies expressing $mHTT_{ex1}$ compared with controls (Fig. S7-1A). Altogether,
85 these results identify *rab5*, *rab7*, and *rab10* as novel injury-response genes in the fly CNS and indicate that
86 neuronal expression of $mHTT_{ex1}$ inhibits injury-induced upregulation of *rab5* and *rab7*.
87 We next examined effects of neuronal $mHTT_{ex1}$ expression on the localization of Rab10, Rab5, and
88 Rab7 proteins endogenously-tagged with YFP-myc at their N-termini, herein referred to as YRab10, YRab5,
89 and YRab7 (Dunst et al., 2015). YRab+ vesicles were identified as YFP+ surfaces with a mean diameter of
90 0.3-8 μm (Fig. S7-1B-G), consistent with vesicle sizes reported in other fly tissues (Prince et al., 2019).
91 Expression of $mHTT_{ex1}$ in Or83b+ ORN axons caused an overall increase in numbers of YRab10+ and YRab7+
92 vesicles, but a decrease in the number of YRab5+ vesicles compared with $wtHTT_{ex1}$ controls (Fig. S7-1H and
93 S7-1I). Further, YRab10+ and YRab7+ vesicles fully or partially overlapped with $mHTT_{ex1}$ signal more often
94 than with $wtHTT_{ex1}$, whereas YRab5+ vesicles were equally associated with each HTT protein (Fig. S7-1I).
95 To test effects of neuronal $mHTT_{ex1}$ aggregates on Rab+ compartments in glia, we expressed YFP-
96 tagged Rab5, 7, and 10 transgenes using a glial-specific Gal4 driver. Expression of $mHTT_{ex1}$ in Or83b+ ORN

97 axons was associated with increased numbers of YFP-Rab10+ and -Rab7+ vesicles, but a decrease in YFP-
98 Rab5+ vesicle abundance, in glia (Fig. 7A,B,G and S7-2A-D). Intriguingly, YFP-Rab10+, -5+, and -7+ vesicles
99 co-localized with neuronal $mHTT_{ex1}$ aggregates to a greater extent than with $wtHTT_{ex1}$ proteins (Fig. 7A,B,H
00 and S7-2A-D, insets), suggesting that $mHTT_{ex1}$ aggregates encounter these Rab+ compartments while
01 transiting the glial phagocytic system. We also expressed YFP-Rab10 transgenes that encode dominant-
02 negative (DN), GDP-locked and constitutively active (CA), GTP-locked variants (Taylor et al., 2015) to test
03 effects of altered Rab10 activity on its localization and interactions with $mHTT_{ex1}$. Interestingly, total and HTT-
04 associated YFP-Rab10(CA)+ vesicles were increased following $mHTT_{ex1}$ expression (Fig. 7E-H), whereas
05 these effects were lost when YFP-Rab10(DN) was expressed in glia (Fig. 7C,D,G,H). Consistent with this, the
06 size of YFP-Rab10+ vesicles associated with $mHTT_{ex1}$ was decreased in glia expressing the DN variant and
07 increased in glia expressing the CA variant (Fig. 7I). These data suggest that Rab10 GTPase activity is
08 correlated with accumulation and enlargement of maturing phagosomes containing $mHTT_{ex1}$ aggregates. We
09 also observed that the mean volume of YFP-Rab7+ vesicles co-localized with $mHTT_{ex1}$ was increased
10 compared with $wtHTT_{ex1}$ controls (Fig. 7I). All together, these data point to accumulation of $mHTT_{ex1}$
11 aggregates within a late phagosome/lysosome compartment as a key mechanism underlying prion-like spread
12 and toxicity in HD.
13

DISCUSSION

Toxic amyloid aggregates have been a primary target in neurodegenerative disease drug development for decades, with some recent promise using immunotherapy to reduce aggregate loads in the brain (Karran and De Strooper, 2022). Microglia and astrocytes have also emerged as attractive therapeutic targets in efforts to boost neuroprotective glial functions or reduce neuroinflammation. However, approaches that target glial cells must effectively strike a balance between amplifying beneficial and reducing harmful effects of these cells in the brain. Here, we tested for interactions between phagocytic glia and pathogenic protein aggregates in a *Drosophila* model of HD. We report that aggregates formed by $mHTT_{ex1}$ protein fragments impair glial transcriptional and functional responses to CNS injury, induce upregulation of stress response and innate immunity genes, and alter numbers of endolysosome vesicles present in uninjured brains. A targeted forward genetic screen revealed that Rab10, a GTPase previously reported to regulate phagosome maturation, mediates prion-like conversion of cytoplasmic $wtHTT_{ex1}$ proteins by phagocytosed $mHTT_{ex1}$ aggregates. Together, these findings suggest that neuronal $mHTT_{ex1}$ aggregates compromise intracellular membrane integrity as they transit endolysosomal systems, perhaps generating toxic, seeding-competent aggregates that propagate disease phenotypes.

Glia respond to neural injury by altering their transcriptional, morphological, and metabolic profiles to promote neuronal survival and clear debris from the brain; however, failure of glia to return to a resting state elicits harmful neuroinflammatory consequences (Liddelow et al., 2020). We have previously reported that active phagocytic glia can have both beneficial (i.e., elimination of toxic aggregates) and harmful (i.e., as vectors for aggregate spread) effects in the brain (Pearce et al., 2015; Donnelly et al., 2020). We report here that key glial injury-responsive pathways, e.g., Draper-mediated phagocytosis and Toll-6-mediated innate immune signaling, are activated in the presence $mHTT_{ex1}$ aggregation in the adult fly brain. These findings are in line with studies from other labs demonstrating that *Drosophila* Toll-6 and mammalian Toll-Like Receptor signaling pathways are upregulated in response to dying neurons during development (McLaughlin et al., 2019) and in patient and mammalian models of neurodegenerative disease (Casula et al., 2011; Miron et al., 2018; Kouli et al., 2020). Interestingly, increased microglial NF-κB signaling mediates tau spread and toxicity in mice, further linking innate immunity to prion-like mechanisms of disease progression (Wang et al., 2022).

41 Thus, activation of glial immune pathways may contribute to feed-forward mechanisms involving aggregate
42 formation, pathology propagation, and neuroinflammatory signaling.

43 Genome-wide association studies have revealed numerous genes associated with increased risk of
44 late-onset AD and other neurodegenerative diseases; strikingly, many of these risk variants are enriched in
45 pathways that control key glial cell functions. For example, rare risk-associated variants of the microglial
46 *TREM2* gene alter amyloid aggregate accumulation and seeding in animal and cell disease models (Leyns et
47 al., 2019; Parhizkar et al., 2019; Jain et al., 2023). A number of additional genes involved in endolysosomal
48 processing are associated with increased risk of AD, PD, FTD, and/or ALS, such as the phagocytic receptor
49 *CD33*, endosome-associated genes *BIN1* and *RIN3*, and *GRN*, the gene that encodes for lysosomal
50 progranulin protein (Podleśny-Drabiniok et al., 2020; Welikovitch et al., 2023). Although Draper/MEGF10
51 variants have not been directly identified as risk factors in neurodegenerative disease, MEGF10 is highly
52 expressed in phagocytic astrocytes (Chung et al., 2013), mediates Aβ aggregate engulfment (Singh et al.,
53 2010; Fujita et al., 2020), and acts as a receptor for C1q, a mediator of early synapse loss in AD mouse
54 models (Hong et al., 2016; Iram et al., 2016). Our finding that upregulation of *draper* and other phagocytic
55 genes is inhibited by $mHTT_{ex1}$ expression suggests that glial responsiveness and phagocytic capacity is
56 attenuated in the presence of protein aggregate pathology in neurons. Genetic risk variants or environmental
57 factors that impact glial health could accelerate these defects and exacerbate aggregate-induced neurotoxicity
58 in the brain.

59 Lysosomes are essential for cell survival, not only to clear damaged or dysfunctional materials from
60 cells, but also as intracellular centers for macromolecule recycling, energy metabolism, and cell-cell
61 communication. Lysosomal abnormalities, including vesicle enlargement, deacidification, and membrane
62 leakiness, have been reported in patient brains and animal and cell models of multiple neurodegenerative
63 diseases, suggesting that lysosome dysfunction plays a central role in disease progression (Bonam et al.,
64 2019; Polanco and Götz, 2022; Udayar et al., 2022). We report here that Rab7+, Rab10+, and Lamp1+
65 phagolysosomes accumulate in glia as a result of $mHTT_{ex1}$ expression in neurons and that a portion of Lamp1+
66 lysosomes are defective in their ability to degrade luminal materials. We also observed that neuronal $mHTT_{ex1}$
67 aggregates were associated with decreased nascent phagosome formation and reduced numbers of early

68 (Rab5+) phagosomes in glia. These findings are consistent with a “traffic jam” model (Small et al., 2017) in
69 which $mHTT_{ex1}$ aggregates accumulate over time in glial endolysosomal compartments, preventing proper flow
70 of materials into (i.e., engulfment) and out of the pathway (i.e., degradation). We postulate that persistence of
71 aggregates in deficient endolysosomes promotes formation and/or release of degradation-resistant aggregates
72 with enhanced toxicity and seeding capacity. This hypothesis is in agreement with recent studies in tauopathy
73 models showing that Aβ aggregation occurs secondary to lysosome deacidification and membrane
74 permeabilization (Lee et al., 2022), and hypophagocytic glia contribute to tau aggregate propagation (Hopp et
75 al., 2018; Brelstaff et al., 2021). Release of seeding-competent aggregates from dysfunctional lysosomes could
76 occur via active exocytosis, in an effort to alleviate cell toxicity, or passively due to vesicle rupture (Flavin et al.,
77 2017; Falcon et al., 2018; Yuste-Checa et al., 2021).

78 Among the growing list of genes linked to neurodegenerative disease pathogenesis are Rab GTPases
79 and genes that modify Rab functions (Kiral et al., 2018). Rab proteins are essential for vesicle sorting and
80 trafficking in all cells and use GTP hydrolysis to differentially associate with and organize intracellular
81 membranes (Homma et al., 2021). In a forward genetic screen aimed at identifying Rabs that regulate
82 phagocytic processing of neuronal $mHTT_{ex1}$ aggregates, we uncovered glial Rab10 as a modifier of prion-like
83 spreading of $mHTT_{ex1}$ from neurons to glia. Interestingly, several other Rab proteins have been previously
84 reported to alter secretion or cell-to-cell propagation of tau or α-synuclein aggregates (Rodriguez et al., 2017;
85 Bae et al., 2018; Ugbode et al., 2019; Rodrigues et al., 2022), suggesting that Rab-dependent processes could
86 be a common mechanism underlying prion-like diseases. Our data suggest that Rab10 acts downstream of
87 Draper to enable engulfed $mHTT_{ex1}$ aggregates to evade lysosomal degradation, perhaps escaping to the
88 cytoplasm during Rab10-dependent intracellular membrane fusion. While relatively understudied compared
89 with other Rabs, Rab10 has been reported to associate with and regulate maturing endo/phagosomes and
90 lysosomes in human macrophages and microglia (Cardoso et al., 2010; Lee et al., 2020). Interestingly, Rab10
91 has already been implicated in multiple neurodegenerative diseases: (1) *RAB10* gene expression is altered in
92 human AD brains (Ridge et al., 2017), (2) rare *RAB10* polymorphisms are linked to protection against AD
93 (Ridge et al., 2017; Tavana et al., 2018), (3) Rab10 depletion is associated with reduced Aβ levels (Udayar et
94 al., 2013; Ridge et al., 2017), and (4) Rab10 is a substrate of the PD risk factor gene leucine-rich repeat kinase

95 2 (LRRK2) (Steger et al., 2016; Seol et al., 2019). Mutant LRRK2-mediated Rab phosphorylation can cause
96 endocytic defects (Liu et al., 2020; Rivero-Ríos et al., 2020; Streubel-Gallasch et al., 2021), and LRRK2-
97 modified Rab10 localizes to and promotes secretion from stressed lysosomes (Eguchi et al., 2018; Kluss et al.,
98 2022). Interestingly, phosphorylated Rab10 (pRab10) levels are elevated in the CNS of AD and PD patients,
99 and pRab10 has been reported to co-localize with pathological tau (Yan et al., 2018; Tezuka et al., 2022)
00 suggesting that post-translational modification of Rab10 modifies the disease state. Whether Rab10's
01 phosphorylation status affects its ability to regulate prion-like activity of $mHTT_{ex1}$ or other amyloid aggregates
02 warrants further investigation.

03 In conclusion, our findings indicate that axonal $mHTT_{ex1}$ aggregates activate glial phagocytosis but also
04 impair normal glial responses to acute neural injury. Aggregate engulfment-induced defects in endolysosomal
05 processing, such as Rab-mediated vesicle membrane fusion, could facilitate the formation and spread of prion-
06 like aggregate seeds in the brain. These findings point to central roles for phagocytic glia in regulating
07 aggregate pathology burden in HD and highlight the importance of exploring therapeutic interventions that
08 target non-neuronal cells.

09

10 **REFERENCES**

11 Alphen, B. van, Stewart, S., Iwanaszko, M., Xu, F., Li, K., Rozenfeld, S., et al. (2022). Glial immune-related
12 pathways mediate effects of closed head traumatic brain injury on behavior and lethality in Drosophila.
13 *PLOS Biology* 20, e3001456. doi: 10.1371/journal.pbio.3001456.

14 Aman, Y., Schmauck-Medina, T., Hansen, M., Morimoto, R. I., Simon, A. K., Bjedov, I., et al. (2021).
15 Autophagy in healthy aging and disease. *Nat Aging* 1, 634–650. doi: 10.1038/s43587-021-00098-4.

16 Bae, E.-J., Kim, D.-K., Kim, C., Mante, M., Adame, A., Rockenstein, E., et al. (2018). LRRK2 kinase regulates
17 α-synuclein propagation via RAB35 phosphorylation. *Nat Commun* 9, 3465. doi: 10.1038/s41467-018-
18 05958-z.

19 Bonam, S. R., Wang, F., and Muller, S. (2019). Lysosomes as a therapeutic target. *Nat Rev Drug Discov* 18,
20 923–948. doi: 10.1038/s41573-019-0036-1.

21 Brand, A. H., and Perrimon, N. (1993). Targeted gene expression as a means of altering cell fates and
22 generating dominant phenotypes | Development | The Company of Biologists. Available at:
23 https://journals.biologists.com/dev/article/118/2/401/37970/Targeted-gene-expression-as-a-means-of-
24 altering [Accessed September 19, 2022].

25 Brelstaff, J. H., Mason, M., Katsinelos, T., McEwan, W. A., Ghetti, B., Tolkovsky, A. M., et al. (2021). Microglia
26 become hypofunctional and release metalloproteases and tau seeds when phagocytosing live neurons
27 with P301S tau aggregates. *Science Advances* 7, eabg4980. doi: 10.1126/sciadv.abg4980.

28 Burbidge, K., Rademacher, D. J., Mattick, J., Zack, S., Grillini, A., Bousset, L., et al. (2022). LGALS3 (galectin
29 3) mediates an unconventional secretion of SNCA/α-synuclein in response to lysosomal membrane
30 damage by the autophagic-lysosomal pathway in human midbrain dopamine neurons. *Autophagy* 18,
31 1020–1048. doi: 10.1080/15548627.2021.1967615.

32 Byrns, C. N., Saikumar, J., and Bonini, N. M. (2021). Glial AP1 is activated with aging and accelerated by
33 traumatic brain injury. *Nat Aging* 1, 585–597. doi: 10.1038/s43587-021-00072-0.

Cardoso, C. M. P., Jordao, L., and Vieira, O. V. (2010). Rab10 regulates phagosome maturation and its overexpression rescues Mycobacterium-containing phagosomes maturation. *Traffic* 11, 221–235. doi: 10.1111/j.1600-0854.2009.01013.x.

Casula, M., Iyer, A. M., Spliet, W. G. M., Anink, J. J., Steentjes, K., Sta, M., et al. (2011). Toll-like receptor signaling in amyotrophic lateral sclerosis spinal cord tissue. *Neuroscience* 179, 233–243. doi: 10.1016/j.neuroscience.2011.02.001.

Chan, C.-C., Scoggin, S., Wang, D., Cherry, S., Dembo, T., Greenberg, B., et al. (2011). Systematic Discovery of Rab GTPases with Synaptic Functions in Drosophila. *Current Biology* 21, 1704–1715. doi: 10.1016/j.cub.2011.08.058.

Chen, S., Berthelier, V., Yang, W., and Wetzel, R. (2001). Polyglutamine aggregation behavior in vitro supports a recruitment mechanism of cytotoxicity11Edited by F. Cohen. *Journal of Molecular Biology* 311, 173–182. doi: 10.1006/jmbi.2001.4850.

Choi, I., Zhang, Y., Seegobin, S. P., Pruvost, M., Wang, Q., Purtell, K., et al. (2020). Microglia clear neuron-released α-synuclein via selective autophagy and prevent neurodegeneration. *Nat Commun* 11, 1386. doi: 10.1038/s41467-020-15119-w.

Chung, W.-S., Clarke, L. E., Wang, G. X., Stafford, B. K., Sher, A., Chakraborty, C., et al. (2013). Astrocytes mediate synapse elimination through MEGF10 and MERTK pathways. *Nature* 504, 394–400. doi: 10.1038/nature12776.

Couto, A., Alenius, M., and Dickson, B. J. (2005). Molecular, Anatomical, and Functional Organization of the Drosophila Olfactory System. *Current Biology* 15, 1535–1547. doi: 10.1016/j.cub.2005.07.034.

Dejanovic, B., Wu, T., Tsai, M.-C., Graykowski, D., Gandham, V. D., Rose, C. M., et al. (2022). Complement C1q-dependent excitatory and inhibitory synapse elimination by astrocytes and microglia in Alzheimer's disease mouse models. *Nat Aging* 2, 837–850. doi: 10.1038/s43587-022-00281-1.

57 Doherty, J., Logan, M. A., Taşdemir, O. E., and Freeman, M. R. (2009). Ensheathing glia function as
58 phagocytes in the adult Drosophila brain. *J Neurosci* 29, 4768–4781. doi: 10.1523/JNEUROSCI.5951-
59 08.2009.

60 Donnelly, K. M., DeLorenzo, O. R., Zaya, A. D., Pisano, G. E., Thu, W. M., Luo, L., et al. (2020). Phagocytic
61 glia are obligatory intermediates in transmission of mutant huntingtin aggregates across neuronal
62 synapses. *eLife* 9, e58499. doi: 10.7554/eLife.58499.

63 Dunlop, J., Jones, P. C., and Finbow, M. E. (1995). Membrane insertion and assembly of ductin: a polytopic
64 channel with dual orientations. *EMBO J* 14, 3609–3616.

65 Dunst, S., Kazimiers, T., von Zadow, F., Jambor, H., Sagner, A., Brankatschk, B., et al. (2015). Endogenously
66 Tagged Rab Proteins: A Resource to Study Membrane Trafficking in Drosophila. *Dev Cell* 33, 351–365.
67 doi: 10.1016/j.devcel.2015.03.022.

68 Duong, L., Radley, H., Lee, B., Dye, D., Pixley, F., Grounds, M., et al. (2021). Macrophage function in the
69 elderly and impact on injury repair and cancer. *Immunity & Ageing* 18, 4. doi: 10.1186/s12979-021-
70 00215-2.

71 Eguchi, T., Kuwahara, T., Sakurai, M., Komori, T., Fujimoto, T., Ito, G., et al. (2018). LRRK2 and its substrate
72 Rab GTPases are sequentially targeted onto stressed lysosomes and maintain their homeostasis. *Proc*
73 *Natl Acad Sci U S A* 115, E9115–E9124. doi: 10.1073/pnas.1812196115.

74 Evans, I. R., Rodrigues, F. S. L. M., Armitage, E. L., and Wood, W. (2015). Draper/CED-1 Mediates an Ancient
75 Damage Response to Control Inflammatory Blood Cell Migration In Vivo. *Curr Biol* 25, 1606–1612. doi:
76 10.1016/j.cub.2015.04.037.

77 Falcon, B., Noad, J., McMahon, H., Randow, F., and Goedert, M. (2018). Galectin-8–mediated selective
78 autophagy protects against seeded tau aggregation. *J Biol Chem* 293, 2438–2451. doi:
79 10.1074/jbc.M117.809293.

80 Finbow, M. E., Goodwin, S. F., Meagher, L., Lane, N. J., Keen, J., Findlay, J. B. C., et al. (1994). Evidence that
81 the 16 kDa proteolipid (subunit c) of the vacuolar H+-ATPase and ductin from gap junctions are the
82 same polypeptide in Drosophila and Manduca: molecular cloning of the Vha16k gene from Drosophila.
83 *Journal of Cell Science* 107, 1817–1824. doi: 10.1242/jcs.107.7.1817.

84 Flavin, W. P., Bousset, L., Green, Z. C., Chu, Y., Skarpathiotis, S., Chaney, M. J., et al. (2017). Endocytic
85 vesicle rupture is a conserved mechanism of cellular invasion by amyloid proteins. *Acta Neuropathol*
86 134, 629–653. doi: 10.1007/s00401-017-1722-x.

87 Fujita, Y., Maeda, T., Sato, C., Sato, M., Hatakeyama, H., Ota, Y., et al. (2020). Engulfment of Toxic Amyloid
88 β-protein in Neurons and Astrocytes Mediated by MEGF10. *Neuroscience* 443, 1–7. doi:
89 10.1016/j.neuroscience.2020.07.016.

90 Ginsberg, S. D., Mufson, E. J., Alldred, M. J., Counts, S. E., Wuu, J., Nixon, R. A., et al. (2011). Upregulation
91 of select rab GTPases in cholinergic basal forebrain neurons in mild cognitive impairment and
92 Alzheimer's disease. *J Chem Neuroanat* 42, 102–110. doi: 10.1016/j.jchemneu.2011.05.012.

93 Hall, A. (1990). The Cellular Functions of Small GTP-Binding Proteins. doi: 10.1126/science.2116664.

94 Han, C., Song, Y., Xiao, H., Wang, D., Franc, N. C., Jan, L. Y., et al. (2014). Epidermal cells are the primary
95 phagocytes in the fragmentation and clearance of degenerating dendrites in Drosophila. *Neuron* 81,
96 544–560. doi: 10.1016/j.neuron.2013.11.021.

97 Heckmann, B. L., Teubner, B. J. W., Tummers, B., Boada-Romero, E., Harris, L., Yang, M., et al. (2019). LC3-
98 associated endocytosis facilitates β-amyloid clearance and mitigates neurodegeneration in murine
99 Alzheimer's Disease. *Cell* 178, 536. doi: 10.1016/j.cell.2019.05.056.

00 Herzog, C., Pons Garcia, L., Keatinge, M., Greenald, D., Moritz, C., Peri, F., et al. (2019). Rapid clearance of
01 cellular debris by microglia limits secondary neuronal cell death after brain injury in vivo. *Development*
02 146, dev174698. doi: 10.1242/dev.174698.

03 Homma, Y., Hiragi, S., and Fukuda, M. (2021). Rab family of small GTPases: an updated view on their
04 regulation and functions. *FEBS J* 288, 36–55. doi: 10.1111/febs.15453.

05 Hong, S., Beja-Glasser, V. F., Nfonoyim, B. M., Frouin, A., Li, S., Ramakrishnan, S., et al. (2016). Complement
06 and microglia mediate early synapse loss in Alzheimer mouse models. *Science* 352, 712–716. doi:
07 10.1126/science.aad8373.

08 Hopp, S. C., Lin, Y., Oakley, D., Roe, A. D., DeVos, S. L., Hanlon, D., et al. (2018). The role of microglia in
09 processing and spreading of bioactive tau seeds in Alzheimer's disease. *J Neuroinflammation* 15, 269.
10 doi: 10.1186/s12974-018-1309-z.

11 Hutagalung, A. H., and Novick, P. J. (2011). Role of Rab GTPases in Membrane Traffic and Cell Physiology.
12 *Physiol Rev* 91, 119–149. doi: 10.1152/physrev.00059.2009.

13 Iram, T., Ramirez-Ortiz, Z., Byrne, M. H., Coleman, U. A., Kingery, N. D., Means, T. K., et al. (2016). Megf10 Is
14 a Receptor for C1Q That Mediates Clearance of Apoptotic Cells by Astrocytes. *J Neurosci* 36, 5185–
15 5192. doi: 10.1523/JNEUROSCI.3850-15.2016.

16 Jain, N., Lewis, C. A., Ulrich, J. D., and Holtzman, D. M. (2023). Chronic TREM2 activation exacerbates Aβ-
17 associated tau seeding and spreading. *J Exp Med* 220, e20220654. doi: 10.1084/jem.20220654.

18 Jeong, G. R., Jang, E.-H., Bae, J. R., Jun, S., Kang, H. C., Park, C.-H., et al. (2018). Dysregulated
19 phosphorylation of Rab GTPases by LRRK2 induces neurodegeneration. *Molecular Neurodegeneration*
20 13, 8. doi: 10.1186/s13024-018-0240-1.

21 Jucker, M., and Walker, L. C. (2018). Propagation and spread of pathogenic protein assemblies in
22 neurodegenerative diseases. *Nat. Neurosci.* 21, 1341–1349. doi: 10.1038/s41593-018-0238-6.

23 Karran, E., and De Strooper, B. (2022). The amyloid hypothesis in Alzheimer disease: new insights from new
24 therapeutics. *Nat Rev Drug Discov* 21, 306–318. doi: 10.1038/s41573-022-00391-w.

25 Kiral, F. R., Kohrs, F. E., Jin, E. J., and Hiesinger, P. R. (2018). Rab GTPases and Membrane Trafficking in
26 Neurodegeneration. *Curr Biol* 28, R471–R486. doi: 10.1016/j.cub.2018.02.010.

Kluss, J. H., Beilina, A., Williamson, C. D., Lewis, P. A., Cookson, M. R., and Bonet-Ponce, L. (2022). Lysosomal positioning regulates Rab10 phosphorylation at LRRK2+ lysosomes. *Proc Natl Acad Sci U S A* 119, e2205492119. doi: 10.1073/pnas.2205492119.

Knowles, T. P. J., Vendruscolo, M., and Dobson, C. M. (2014). The amyloid state and its association with protein misfolding diseases. *Nat Rev Mol Cell Biol* 15, 384–396. doi: 10.1038/nrm3810.

Kohrs, F. E., Daumann, I.-M., Pavlovic, B., Jin, E. J., Kiral, F. R., Lin, S.-C., et al. (2021). Systematic functional analysis of rab GTPases reveals limits of neuronal robustness to environmental challenges in flies. *eLife* 10, e59594. doi: 10.7554/eLife.59594.

Kouli, A., Camacho, M., Allinson, K., and Williams-Gray, C. H. (2020). Neuroinflammation and protein pathology in Parkinson's disease dementia. *Acta Neuropathologica Communications* 8, 211. doi: 10.1186/s40478-020-01083-5.

Krasemann, S., Madore, C., Cialic, R., Baufeld, C., Calcagno, N., El Fatimy, R., et al. (2017). The TREM2-APOE Pathway Drives the Transcriptional Phenotype of Dysfunctional Microglia in Neurodegenerative Diseases. *Immunity* 47, 566-581.e9. doi: 10.1016/j.immuni.2017.08.008.

Langemeyer, L., Fröhlich, F., and Ungermann, C. (2018). Rab GTPase Function in Endosome and Lysosome Biogenesis. *Trends in Cell Biology* 28, 957–970. doi: 10.1016/j.tcb.2018.06.007.

Larsson, M. C., Domingos, A. I., Jones, W. D., Chiappe, M. E., Amrein, H., and Vosshall, L. B. (2004). Or83b Encodes a Broadly Expressed Odorant Receptor Essential for Drosophila Olfaction. *Neuron* 43, 703–714. doi: 10.1016/j.neuron.2004.08.019.

Lee, H., Flynn, R., Sharma, I., Haberman, E., Carling, P. J., Nicholls, F. J., et al. (2020). LRRK2 Is Recruited to Phagosomes and Co-recruits RAB8 and RAB10 in Human Pluripotent Stem Cell-Derived Macrophages. *Stem Cell Reports* 14, 940–955. doi: 10.1016/j.stemcr.2020.04.001.

49 Lee, J.-H., Kim, J.-Y., Noh, S., Lee, H., Lee, S. Y., Mun, J. Y., et al. (2021). Astrocytes phagocytose adult
50 hippocampal synapses for circuit homeostasis. *Nature* 590, 612–617. doi: 10.1038/s41586-020-03060-
51 3.

52 Lee, J.-H., Yang, D.-S., Goulbourne, C. N., Im, E., Stavrides, P., Pensalfini, A., et al. (2022). Faulty
53 autolysosome acidification in Alzheimer's disease mouse models induces autophagic build-up of Aβ in
54 neurons, yielding senile plaques. *Nat Neurosci* 25, 688–701. doi: 10.1038/s41593-022-01084-8.

55 Leyns, C. E. G., Gratuze, M., Narasimhan, S., Jain, N., Koscal, L. J., Jiang, H., et al. (2019). TREM2 function
56 impedes tau seeding in neuritic plaques. *Nat Neurosci* 22, 1217–1222. doi: 10.1038/s41593-019-0433-
57 0.

58 Liddelow, S. A., Guttenplan, K. A., Clarke, L. E., Bennett, F. C., Bohlen, C. J., Schirmer, L., et al. (2017).
59 Neurotoxic reactive astrocytes are induced by activated microglia. *Nature* 541, 481–487. doi:
60 10.1038/nature21029.

61 Liddelow, S. A., Marsh, S. E., and Stevens, B. (2020). Microglia and Astrocytes in Disease: Dynamic Duo or
62 Partners in Crime? *Trends Immunol* 41, 820–835. doi: 10.1016/j.it.2020.07.006.

63 Liu, C.-C., Hu, J., Zhao, N., Wang, J., Wang, N., Cirrito, J. R., et al. (2017). Astrocytic LRP1 Mediates Brain Aβ
64 Clearance and Impacts Amyloid Deposition. *J Neurosci* 37, 4023–4031. doi:
65 10.1523/JNEUROSCI.3442-16.2017.

66 Liu, Z., Xu, E., Zhao, H. T., Cole, T., and West, A. B. (2020). LRRK2 and Rab10 coordinate macropinocytosis
67 to mediate immunological responses in phagocytes. *EMBO J* 39, e104862. doi:
68 10.15252/embj.2020104862.

69 MacDonald, J. M., Beach, M. G., Porpiglia, E., Sheehan, A. E., Watts, R. J., and Freeman, M. R. (2006). The
70 Drosophila Cell Corpse Engulfment Receptor Draper Mediates Glial Clearance of Severed Axons.
71 *Neuron* 50, 869–881. doi: 10.1016/j.neuron.2006.04.028.

72 Magaki, S. D., Williams, C. K., and Vinters, H. V. (2018). Glial function (and dysfunction) in the normal &
73 ischemic brain. *Neuropharmacology* 134, 218–225. doi: 10.1016/j.neuropharm.2017.11.009.

74 McGuire, S. E., Le, P. T., and Davis, R. L. (2001). The Role of Drosophila Mushroom Body Signaling in
75 Olfactory Memory. *Science* 293, 1330–1333. doi: 10.1126/science.1062622.

76 McLaughlin, C. N., Perry-Richardson, J. J., Coutinho-Budd, J. C., and Broihier, H. T. (2019). Dying neurons
77 utilize innate immune signaling to prime glia for phagocytosis during development. *Dev Cell* 48, 506-
78 522.e6. doi: 10.1016/j.devcel.2018.12.019.

79 Miesenböck, G., De Angelis, D. A., and Rothman, J. E. (1998). Visualizing secretion and synaptic transmission
80 with pH-sensitive green fluorescent proteins. *Nature* 394, 192–195. doi: 10.1038/28190.

81 Miron, J., Picard, C., Frappier, J., Dea, D., Théroux, L., and Poirier, J. (2018). TLR4 Gene Expression and Pro-
82 Inflammatory Cytokines in Alzheimer's Disease and in Response to Hippocampal Deafferentation in
83 Rodents. *Journal of Alzheimer's Disease* 63, 1547–1556. doi: 10.3233/JAD-171160.

84 Monaco, A., and Fraldi, A. (2020). Protein Aggregation and Dysfunction of Autophagy-Lysosomal Pathway: A
85 Vicious Cycle in Lysosomal Storage Diseases. *Front Mol Neurosci* 13, 37. doi:
86 10.3389/fnmol.2020.00037.

87 Neniskyte, U., Neher, J. J., and Brown, G. C. (2011). Neuronal Death Induced by Nanomolar Amyloid β Is
88 Mediated by Primary Phagocytosis of Neurons by Microglia*. *Journal of Biological Chemistry* 286,
89 39904–39913. doi: 10.1074/jbc.M111.267583.

90 Ng, E. L., and Tang, B. L. (2008). Rab GTPases and their roles in brain neurons and glia. *Brain Research*
91 *Reviews* 58, 236–246. doi: 10.1016/j.brainresrev.2008.04.006.

92 Paolicelli, R. C., Bolasco, G., Pagani, F., Maggi, L., Scianni, M., Panzanelli, P., et al. (2011). Synaptic pruning
93 by microglia is necessary for normal brain development. *Science* 333, 1456–1458. doi:
94 10.1126/science.1202529.

95 Parhizkar, S., Arzberger, T., Brendel, M., Kleinberger, G., Deussing, M., Focke, C., et al. (2019). Loss of
96 TREM2 function increases amyloid seeding but reduces plaque-associated ApoE. *Nat Neurosci* 22,
97 191–204. doi: 10.1038/s41593-018-0296-9.

98 Pearce, M. M. P., Spartz, E. J., Hong, W., Luo, L., and Kopito, R. R. (2015). Prion-like transmission of neuronal
99 huntingtin aggregates to phagocytic glia in the Drosophila brain. *Nat Commun* 6, 6768. doi:
00 10.1038/ncomms7768.

01 Podleśny-Drabiniok, A., Marcora, E., and Goate, A. M. (2020). Microglial Phagocytosis: A Disease-Associated
02 Process Emerging from Alzheimer's Disease Genetics. *Trends Neurosci* 43, 965–979. doi:
03 10.1016/j.tins.2020.10.002.

04 Poe, A. R., Wang, B., Sapar, M. L., Ji, H., Li, K., Onabajo, T., et al. (2019). Robust CRISPR/Cas9-Mediated
05 Tissue-Specific Mutagenesis Reveals Gene Redundancy and Perdurance in Drosophila. *Genetics* 211,
06 459–472. doi: 10.1534/genetics.118.301736.

07 Polanco, J. C., and Götz, J. (2022). Exosomal and vesicle-free tau seeds—propagation and convergence in
08 endolysosomal permeabilization. *The FEBS Journal* 289, 6891–6907. doi: 10.1111/febs.16055.

09 Portela, M., Yang, L., Paul, S., Li, X., Veraksa, A., Parsons, L. M., et al. (2018). Lgl reduces endosomal vesicle
10 acidification and Notch signaling by promoting the interaction between Vap33 and the V-ATPase
11 complex. *Sci Signal* 11, eaar1976. doi: 10.1126/scisignal.aar1976.

12 Potter, C. J., and Luo, L. (2011). Using the Q system in Drosophila. *Nat Protoc* 6, 1105–1120. doi:
13 10.1038/nprot.2011.347.

14 Preisinger, E., Jordan, B. M., Kazantsev, A., and Housman, D. (1999). Evidence for a recruitment and
15 sequestration mechanism in Huntington's disease. *Philos Trans R Soc Lond B Biol Sci* 354, 1029–
16 1034. doi: 10.1098/rstb.1999.0455.

17 Prince, E., Kroeger, B., Gligorov, D., Wilson, C., Eaton, S., Karch, F., et al. (2019). Rab-mediated trafficking in
18 the secondary cells of Drosophila male accessory glands and its role in fecundity. *Traffic* 20, 137–151.
19 doi: 10.1111/tra.12622.

20 Pulipparacharuvil, S., Akbar, M. A., Ray, S., Sevrioukov, E. A., Haberman, A. S., Rohrer, J., et al. (2005).
21 Drosophila Vps16A is required for trafficking to lysosomes and biogenesis of pigment granules. *Journal*
22 *of Cell Science* 118, 3663–3673. doi: 10.1242/jcs.02502.

23 Purice, M. D., Ray, A., Münzel, E. J., Pope, B. J., Park, D. J., Speese, S. D., et al. (2017). A novel Drosophila
24 injury model reveals severed axons are cleared through a Draper/MMP-1 signaling cascade. *eLife* 6,
25 e23611. doi: 10.7554/eLife.23611.

26 Raiders, S., Han, T., Scott-Hewitt, N., Kucenas, S., Lew, D., Logan, M. A., et al. (2021). Engulfed by Glia: Glial
27 Pruning in Development, Function, and Injury across Species. *J. Neurosci.* 41, 823–833. doi:
28 10.1523/JNEUROSCI.1660-20.2020.

29 Ray, A., Speese, S. D., and Logan, M. A. (2017). Glial Draper Rescues Aβ Toxicity in a Drosophila Model of
30 Alzheimer's Disease. *J Neurosci* 37, 11881–11893. doi: 10.1523/JNEUROSCI.0862-17.2017.

31 Ridge, P. G., Karch, C. M., Hsu, S., Arano, I., Teerlink, C. C., Ebbert, M. T. W., et al. (2017). Linkage, whole
32 genome sequence, and biological data implicate variants in RAB10 in Alzheimer's disease resilience.
33 *Genome Med* 9, 100. doi: 10.1186/s13073-017-0486-1.

34 Rivero-Ríos, P., Romo-Lozano, M., Fernández, B., Fdez, E., and Hilfiker, S. (2020). Distinct Roles for RAB10
35 and RAB29 in Pathogenic LRRK2-Mediated Endolysosomal Trafficking Alterations. *Cells* 9, 1719. doi:
36 10.3390/cells9071719.

37 Rodrigues, P. V., de Godoy, J. V. P., Bosque, B. P., Amorim Neto, D. P., Tostes, K., Palameta, S., et al.
38 (2022). Transcellular propagation of fibrillar α-synuclein from enteroendocrine to neuronal cells requires
39 cell-to-cell contact and is Rab35-dependent. *Sci Rep* 12, 4168. doi: 10.1038/s41598-022-08076-5.

40 Rodriguez, L., Mohamed, N.-V., Desjardins, A., Lippé, R., Fon, E. A., and Leclerc, N. (2017). Rab7A regulates
41 tau secretion. *J Neurochem* 141, 592–605. doi: 10.1111/jnc.13994.

42 Rong, Y., McPhee, C. K., Deng, S., Huang, L., Chen, L., Liu, M., et al. (2011). Spinster is required for
43 autophagic lysosome reformation and mTOR reactivation following starvation. *Proc Natl Acad Sci U S*
44 *A* 108, 7826–7831. doi: 10.1073/pnas.1013800108.

45 Santra, M., Dill, K. A., and de Graff, A. M. R. (2019). Proteostasis collapse is a driver of cell aging and death.
46 *Proceedings of the National Academy of Sciences* 116, 22173–22178. doi: 10.1073/pnas.1906592116.

47 Scherzinger, E., Sittler, A., Schweiger, K., Heiser, V., Lurz, R., Hasenbank, R., et al. (1999). Self-assembly of
48 polyglutamine-containing huntingtin fragments into amyloid-like fibrils: Implications for Huntington's
49 disease pathology. *Proc Natl Acad Sci U S A* 96, 4604–4609.

50 Seol, W., Nam, D., and Son, I. (2019). Rab GTPases as Physiological Substrates of LRRK2 Kinase. *Exp*
51 *Neurobiol* 28, 134–145. doi: 10.5607/en.2019.28.2.134.

52 Seto, S., Tsujimura, K., and Koide, Y. (2011). Rab GTPases regulating phagosome maturation are differentially
53 recruited to mycobacterial phagosomes. *Traffic* 12, 407–420. doi: 10.1111/j.1600-0854.2011.01165.x.

54 Singh, T. D., Park, S.-Y., Bae, J., Yun, Y., Bae, Y.-C., Park, R.-W., et al. (2010). MEGF10 functions as a
55 receptor for the uptake of amyloid-β. *FEBS Letters* 584, 3936–3942. doi: 10.1016/j.febslet.2010.08.050.

56 Small, S. A., Simoes-Spassov, S., Mayeux, R., and Petsko, G. A. (2017). Endosomal traffic jams represent a
57 pathogenic hub and therapeutic target in Alzheimer's disease. *Trends Neurosci* 40, 592–602. doi:
58 10.1016/j.tins.2017.08.003.

59 Steger, M., Tonelli, F., Ito, G., Davies, P., Trost, M., Vetter, M., et al. (2016). Phosphoproteomics reveals that
60 Parkinson's disease kinase LRRK2 regulates a subset of Rab GTPases. *Elife* 5, e12813. doi:
61 10.7554/eLife.12813.

62 Stein, K. C., Morales-Polanco, F., van der Lienden, J., Rainbolt, T. K., and Frydman, J. (2022). Ageing
63 exacerbates ribosome pausing to disrupt cotranslational proteostasis. *Nature* 601, 637–642. doi:
64 10.1038/s41586-021-04295-4.

65 Streubel-Gallasch, L., Giusti, V., Sandre, M., Tessari, I., Plotegher, N., Giusto, E., et al. (2021). Parkinson's
66 Disease–Associated LRRK2 Interferes with Astrocyte-Mediated Alpha-Synuclein Clearance. *Mol*
67 *Neurobiol* 58, 3119–3140. doi: 10.1007/s12035-021-02327-8.

68 Tavana, J. P., Rosene, M., Jensen, N. O., Ridge, P. G., Kauwe, J. S., and Karch, C. M. (2018). RAB10: an
69 Alzheimer's disease resilience locus and potential drug target. *Clin Interv Aging* 14, 73–79. doi:
70 10.2147/CIA.S159148.

71 Taylor, C. A., Yan, J., Howell, A. S., Dong, X., and Shen, K. (2015). RAB-10 Regulates Dendritic Branching by
72 Balancing Dendritic Transport. *PLoS Genet* 11, e1005695. doi: 10.1371/journal.pgen.1005695.

73 Tezuka, T., Taniguchi, D., Sano, M., Shimada, T., Oji, Y., Tsunemi, T., et al. (2022). Pathophysiological
74 evaluation of the LRRK2 G2385R risk variant for Parkinson's disease. *npj Parkinsons Dis.* 8, 1–7. doi:
75 10.1038/s41531-022-00367-y.

76 Udayar, V., Buggia-Prévot, V., Guerreiro, R. L., Siegel, G., Rambabu, N., Soohoo, A. L., et al. (2013). A Paired
77 RNAi and RabGAP Overexpression Screen Identifies Rab11 as a Regulator of β-Amyloid Production.
78 *Cell Rep* 5, 1536–1551. doi: 10.1016/j.celrep.2013.12.005.

79 Udayar, V., Chen, Y., Sidransky, E., and Jagasia, R. (2022). Lysosomal dysfunction in neurodegeneration:
80 emerging concepts and methods. *Trends in Neurosciences* 45, 184–199. doi:
81 10.1016/j.tins.2021.12.004.

82 Ugbode, C., Fort-Aznar, L., and Sweeney, S. T. (2019). Leaky endosomes push tau over the seed limit.
83 *Journal of Biological Chemistry* 294, 18967–18968. doi: 10.1074/jbc.H119.011687.

84 Vieira, O. V., Botelho, R. J., and Grinstein, S. (2002). Phagosome maturation: aging gracefully. *Biochem J* 366,
85 689–704. doi: 10.1042/BJ20020691.

86 Wakida, N. M., Cruz, G. M. S., Ro, C. C., Moncada, E. G., Khatibzadeh, N., Flanagan, L. A., et al. (2018).
87 Phagocytic response of astrocytes to damaged neighboring cells. *PLOS ONE* 13, e0196153. doi:
88 10.1371/journal.pone.0196153.

89 Wang, C., Fan, L., Khawaja, R. R., Liu, B., Zhan, L., Kodama, L., et al. (2022). Microglial NF-κB drives tau
90 spreading and toxicity in a mouse model of tauopathy. *Nat Commun* 13, 1969. doi: 10.1038/s41467-
91 022-29552-6.

92 Wang, Y., Arnold, M. L., Smart, A. J., Wang, G., Androwski, R. J., Morera, A., et al. (2023). Large vesicle
93 extrusions from C. elegans neurons are consumed and stimulated by glial-like phagocytosis activity of
94 the neighboring cell. *eLife* 12, e82227. doi: 10.7554/eLife.82227.

95 Wanker, E. E. (2000). Protein Aggregation and Pathogenesis of Huntingtons Disease: Mechanisms and
96 Correlations. 381, 937–942. doi: 10.1515/BC.2000.114.

97 Welikovitch, L. A., Dujardin, S., Dunn, A. R., Fernandes, A. R., Khasnavis, A., Chibnik, L. B., et al. (2023). Rate
98 of tau propagation is a heritable disease trait in genetically diverse mouse strains. *iScience* 26, 105983.
99 doi: 10.1016/j.isci.2023.105983.

00 Wodrich, A. P. K., Scott, A. W., Shukla, A. K., Harris, B. T., and Giniger, E. (2022). The Unfolded Protein
01 Responses in Health, Aging, and Neurodegeneration: Recent Advances and Future Considerations.
02 *Front Mol Neurosci* 15, 831116. doi: 10.3389/fnmol.2022.831116.

03 Yan, T., Wang, L., Gao, J., Siedlak, S. L., Huntley, M. L., Termsarasab, P., et al. (2018). Rab10
04 Phosphorylation is a Prominent Pathological Feature in Alzheimer's Disease. *J Alzheimers Dis* 63,
05 157–165. doi: 10.3233/JAD-180023.

06 Yan, Y., Denef, N., and Schüpbach, T. (2009). The vacuolar proton pump (V-ATPase) is required for Notch
07 signaling and endosomal trafficking in Drosophila. *Dev Cell* 17, 387–402. doi:
08 10.1016/j.devcel.2009.07.001.

09 Yuste-Checa, P., Trinkaus, V. A., Riera-Tur, I., Imamoglu, R., Schaller, T. F., Wang, H., et al. (2021). The
10 extracellular chaperone Clusterin enhances Tau aggregate seeding in a cellular model. *Nat Commun*
11 12, 4863. doi: 10.1038/s41467-021-25060-1.

12 Zhang, J., Schulze, K. L., Hiesinger, P. R., Suyama, K., Wang, S., Fish, M., et al. (2007). Thirty-One Flavors of
13 Drosophila Rab Proteins. *Genetics* 176, 1307–1322. doi: 10.1534/genetics.106.066761.

14 Zheng, B., and Tuszynski, M. H. (2023). Regulation of axonal regeneration after mammalian spinal cord injury.
15 *Nat Rev Mol Cell Biol* 24, 396–413. doi: 10.1038/s41580-022-00562-y.

16

17

18 **FIGURE LEGENDS**

19 **Figure 1. mHTT expression in neurons and glia impairs clearance of injured axons**. (**A-B**) Maximum
20 intensity projections of mCD8-GFP-labeled DA1 ORN axons expressing (**A**) HTT_{ex1}Q25- or (**B**) HTT_{ex1}Q91-
21 mCherry in 7 day-old uninjured flies (*top*) or 14 day-old flies subjected to bilateral antennal nerve axotomy 7
22 days earlier (*bottom*). Scale bars = 5μm. (**C-D**) Quantification of (**C**) mCD8-GFP+ and (**D**) HTT_{ex1}-mCherry+
23 DA1 ORN axons remaining in 7 day-old, 14 day-old, and 28 day-old uninjured flies or flies at 1, 3, and 5 days
24 post-injury. Data were normalized to the uninjured condition for each genotype and age and graphed as
25 mean±s.e.m.; *p<0.05, **p<0.01, ***p<0.001 by unpaired 2-tailed t-test; n≥16. (**E-F**) Maximum intensity
26 projections of mCD8-GFP-labeled DA1 ORN axons in 1 day-old flies expressing (**E**) HTT_{ex1}Q25- or (**F**)
27 HTT_{ex1}Q91-V5 in all glia. Scale bars = 5μm. (**G**) Quantification of mCD8-GFP+ DA1 ORN axons in uninjured
28 flies and flies at 1 and 3 days post-injury. Data were normalized to the uninjured condition for each genotype
29 and graphed as mean±s.e.m.; ***p<0.001, unpaired 2-tailed t-test; n≥16.

30

31 **Figure 2. mHTT expression inhibits engulfment of injured ORN axons.** (**A-B**) Maximum intensity
32 projections of VA1lm ORN axons co-expressing the ratiometric phagocytic indicator, MApHS (transgene shown
33 above images), and (**A**) HTT_{ex1}Q25- or (**B**) HTT_{ex1}Q91-V5 from 7 day-old uninjured flies (*left*) and flies 25 hours
34 post-injury (*right*). Scale bars = 10μm. (**C**) pHluorin:tdTomato fluorescence intensity ratios calculated in VA1lm
35 glomeruli from 7-day-old uninjured flies and flies at 14 or 25 hours post-injury. Data were normalized to the
36 uninjured condition for each genotype. (**D**) pHluorin:tdTomato fluorescence intensity ratios in 7 day-old flies co-
37 expressing MApHS with HTT_{ex1}Q25- or HTT_{ex1}Q91-V5 in VA1lm ORNs, normalized to wtHTT controls. Data
38 are shown as mean±s.e.m.; **p<0.01, ***p<0.001, ****p<0.0001 by unpaired 2-tailed t-test; n≥15. (**E-F**)
39 Maximum intensity projections of VA1lm ORN axons co-expressing mutant HTT_{ex1}Q91-associated pH sensor
40 (mHApHS) (transgene shown above images) and (**E**) repo-Cas9 or (**F**) repo-Cas9 and gRNAs targeting *draper*
41 ("Draper KO"). Scale bars = 5μm. (**G**) pHluorin:tdTomato fluorescence intensity ratios calculated in VA1lm
42 glomeruli from 9-10 day-old flies seen in (**E-F**). Data normalized to flies not expressing gRNAs. Data are shown
43 as mean±s.e.m.; **p<0.01 by unpaired 2-tailed t-test; n≥16.

44

45 **Figure 3. mHTT expression in ORNs upregulates phagocytic and innate immunity genes and impairs**
46 **injury-induced transcriptional responses. (A)** qPCR analysis of the indicated genes in 8-11 day-old flies
47 expressing GFP, HTT_{ex1}Q25-, or HTT_{ex1}Q91-GFP in Or83b+ ORNs. RNA was isolated from heads of uninjured
48 flies or flies 3 hours after bilateral antennal and maxillary palp nerve injury. Data are shown as mean±s.e.m
49 and normalized to the housekeeping gene *rpl32*. *p<0.05, **p<0.01, ***p<0.001 by one-way ANOVA, asterisks
50 and hashtags indicate statistical significance comparing -/+ injury or genotypes, respectively; n=3. (**B**)
51 Diagrams of Draper (blue) and Toll-6 (purple) signaling pathways. (**C-H**) Maximum intensity projections of
52 Or83b+ ORN axons from 14-15 day-old flies expressing (**C,F**) HTT_{ex1}Q25- or (**D,G**) HTT_{ex1}Q91-V5 in (**C-D**)
53 Toll6-GFP or (**F-G**) Jra-GFP genetic backgrounds. Brains were immunostained with GFP, V5, or N-Cadherin
54 antibodies. Scale bars = 10μm. (**E,H**) Quantification of (**E**) Toll6-GFP or (**H**) Jra-GFP expression from flies
55 show in (**C-D** and **F-G**). Data are graphed as mean±s.e.m.; *p<0.05, ****p<0.0001 by unpaired 2-tailed t-test;
56 n≥15.

57

58 **Figure 4. Glial innate immunity genes regulate numbers of mHTT aggregates in ORN axons. (A**)
59 Maximum intensity projections of DA1 glomeruli from 7 day-old flies expressing HTT_{ex1}Q91-mCherry in DA1
60 ORNs and siRNAs targeting the indicated genes in ensheathing glia. Scale bars = 5μm. (**B)** Quantification of
61 HTT_{ex1}Q91-mCherry aggregates detected in DA1 glomeruli from flies shown in (**A**). Data are shown as
62 mean±s.e.m.; *p<0.05, **p<0.01, ****p<0.0001 by one-way ANOVA, comparing each genotype to no RNAi or
63 $mCherry^{RNAi}$ controls; n≥16. (**C**) Maximum intensity projections of DA1 glomeruli from 7 day-old flies expressing
64 HTT_{ex1}Q91-mCherry in DA1 ORNs and siRNAs targeting mCherry or Ets21c in repo+ glia in the presence of
65 tubP-$Gal80^{ts}$. Adult flies were raised at the permissive (18°C, *top*) or restrictive (29°C, *bottom*) temperatures to
66 restrict siRNA expression in adults. Scale bars = 5μm. (**D**) Quantification of HTT_{ex1}Q91-mCherry aggregates
67 detected in DA1 glomeruli from flies shown in (**C**). Data are shown as mean±s.e.m.; ****p<0.0001 by one-way
68 ANOVA; n≥16.

69

70 **Figure 5. Lysosome accumulation in fly brains expressing mHTT in ORNs. (A-B**) Confocal stacks
71 showing antennal lobes from 19-22 day-old flies expressing (**A**) HTT_{ex1}Q25- or (**B**) HTT_{ex1}Q91-mCherry in

72 Or83b+ ORNs and LAMP1 tagged at its cytoplasmic C-terminus with GFP (LAMP1-GFP) in glia. LAMP1-GFP+
73 or HTT+ surfaces identified by semi-automated image segmentation are shown to the right of each set of raw
74 fluorescence images. Fluorescence signal of $HTT_{ex1}Q25$ adjusted for easier visualization. Insets show
75 magnified regions of interest from each image. LAMP1-GFP surfaces isolated to highlight individual
76 compartment associating with one or more HTT surfaces. Scale bars = 10μm. (**C-D**) Quantification of (**C**)
77 LAMP1-GFP+ surfaces and (**D**) LAMP1-GFP+ surfaces that co-localized with HTT. Data are shown as
78 mean±s.e.m.; *p<0.05, ****p<0.0001 by unpaired 2-tailed t-test; n≥20. (**E**) Quantification of LAMP1-GFP+
79 surface volume in brains expressing $HTT_{ex1}Q25$- or $HTT_{ex1}Q91$-mCherry. The third bar represents LAMP1-
80 GFP+ surfaces that co-localized with $mHTT_{ex1}$. Data are shown as mean±s.e.m.; ***p<0.001 by unpaired 2-
81 tailed t-test; n≥20. **(F-G**) Confocal stacks showing antennal lobes from 21-22 day-old flies (**F**) $HTT_{ex1}Q25$- or
82 (**G**) $HTT_{ex1}Q91$-mCherry in Or83b+ ORNs and LAMP1 tagged at its luminal N-terminus with GFP (GFP-
83 LAMP1) in glia. GFP-LAMP1+ or HTT+ surfaces identified by semi-automated image segmentation are shown
84 to the right of each set of raw fluorescence images. Fluorescence signal of $HTT_{ex1}Q25$ adjusted for easier
85 visualization. Insets show magnified regions of interest from each image. GFP-LAMP1 surfaces isolated to
86 highlight individual compartment associating with one or more HTT surfaces. Scale bars = 10μm. (**H-I**)
87 Quantification of (**H**) GFP-LAMP1+ surfaces and (**I**) GFP-LAMP1+ surfaces that co-localized with HTT. Data
88 are shown as mean±s.e.m.; ***p<0.001, ****p<0.0001 by unpaired 2-tailed t-test; n≥16. (**J**) Quantification of
89 GFP-LAMP1+ surface volume in brains expressing $HTT_{ex1}Q25$- or $HTT_{ex1}Q91$-mCherry. The third bar
90 represents GFP-LAMP1+ surfaces that co-localized with $mHTT_{ex1}$. Data are shown as mean±s.e.m.; **p<0.01
91 by unpaired 2-tailed t-test; n≥16.

92

93 **Figure 6. Rab10 is required for prion-like conversion of glial wtHTT by neuronal mHTT aggregates. (A**)
94 Confocal stacks of DA1 glomeruli from 7 day-old flies expressing $HTT_{ex1}Q91$-mCherry in DA1 ORNs and
95 $HTT_{ex1}Q25$-GFP plus siRNAs targeting firefly luciferase (FFLuc), Draper, or Rab10 in repo+ glia. Surfaces
96 representing mHTT aggregates (*red*) and seeded wtHTT+mHTT aggregates are superimposed on the raw
97 data. Scale bars = 5μm. (**B-C**) mHTT (**B**) or mHTT+wtHTT (**C**) aggregates quantified from flies expressing
98 $HTT_{ex1}Q91$-mCherry in DA1 ORNs and $HTT_{ex1}Q25$-GFP plus siRNAs targeting 23 different Rab GTPases or

99 Draper-I in repo+ glia. Negative controls expressed no siRNAs or siRNAs targeting FFLuc or mCherry (*black*
00 *bars*). Data are shown as mean±s.e.m.; *p<0.05, ***p<0.005 by one-way ANOVA comparing to controls
01 expressing FFLuc siRNAs; n≥7. (**D-E**) Quantification of (**D**) mHTT or (**E**) mHTT+wtHTT aggregates from 10
02 day-old flies expressing HTT_{ex1}Q91-mCherry in DA1 ORNs and HTT_{ex1}Q25-GFP in DA1 PNs, either
03 heterozygous or trans-heterozygous for *draper* (*drpr/*+), *rab10* (*rab10/*+), or *rab14* (*rab14/*+) mutant alleles.
04 Data are shown as mean±s.e.m.; *p<0.05 by one-way ANOVA; n≥8.

05

06 **Figure 7. Association of neuronal mHTT aggregates with glial Rab GTPases that label early, maturing,**
07 **and late phagosomes.** (**A-F**) Confocal stacks of the antennal lobe from 16-19 day-old flies expressing (**A, C,**
08 **E**) HTT_{ex1}Q25- or (**B, D, F**) HTT_{ex1}Q91-V5 in Or83b+ ORNs and (**A-B**) YFP-Rab10 (T23N), (**C-D**) YFP-Rab10
09 (wt), or (**E-F**) YFP-Rab10 (Q68L) in glia. Rab+ or HTT+ surfaces identified by semi-automated image
10 segmentation are shown to the right of each set of raw fluorescence images. Fluorescence signal of
11 HTT_{ex1}Q25 adjusted for easier visualization. Insets show magnified regions of interest. YFP-Rab surfaces
12 isolated to highlight individual compartment associating with one or more HTT surfaces. Scale bars = 10μm.
13 (**G-H**) Quantification of (**G**) Rab+ surfaces and (**H**) Rab+ surfaces that co-localized with HTT for Rab10 (T23N),
14 Rab10 (wt), Rab10 (Q68L), Rab5, and Rab7 conditions. **I**) Quantification of Rab+ surface volume (μm^3) and
15 Rab+ surfaces co-localized with $mHTT_{ex1}$ surfaces (mHTT+/Rab+) for Rab10 (T23N), Rab10 (wt), Rab10
16 (Q68L), Rab5, and Rab7 conditions. Data are shown as mean±s.e.m.; *p<0.05, **p<0.01, ***p<0.001,
17 ****p<0.0001 by unpaired 2-tailed t-test; n≥16.

18

SUPPLEMENTAL FIGURE AND TABLE LEGENDS

Supplemental Figure S1. mHTT expression is associated with reduced ORN axon abundance. (**A-B**) Quantification of mCD8-GFP+ DA1 ORN axons in 1, 7, 14, and 28 day-old flies expressing HTT_{ex1}Q25- or HTT_{ex1}Q91-mCherry in (**A**) DA1 ORNs or (**B**) repo+ glia. Data are shown as mean±s.e.m.; ****p<0.0001 by unpaired 2-tailed t-test. (**C-D**) Maximum intensity projections of antennal lobes from 5-6 day-old flies expressing (**C**) HTT_{ex1}Q25- or (**D**) HTT_{ex1}Q91-V5 in glia and immunostained with antibodies against the V5 epitope tag. Scale bars = 10μm.

Supplemental Figure S2. (A-B, D-E) Maximum intensity projections of (**A-B**) Or83b+ ORN axons or (**D-E**) OK107+ MBN soma expressing (**A,D**) HTT_{ex1}Q25- or (**B,E**) HTT_{ex1}Q91-associated pH sensor (HApHS) from 13-14 day-old flies. Scale bars = 10μm. (**C,F**) Quantification of data shown in (**A-B** and **D-E**), normalized to wtHTT controls. Data are shown as mean±s.e.m.; ***p<0.001, ****p<0.0001 by unpaired 2-tailed t-test; n≥15. (**G-H**) Maximum intensity projections of the central brain of 6-7 day-old flies expressing (**G**) repo-Cas9 and (**H**) repo-Cas9 plus gRNAs targeting *draper*. Brains were immunostained with anti-Draper. Scale bars = 10μm. (**I**) Quantification of Draper immunofluorescence in brains from flies shown in (**G-H**). Data are shown as mean±s.e.m.; ****p<0.0001 by unpaired 2-tailed t-test; n≥10.

Supplemental Fig S4. Prion-like spreading of neuronal mHTT aggregates to ensheathing glia. (**A-C**) Maximum intensity projections of DA1 glomeruli from 4-5 day-old flies expressing HTT_{ex1}Q91-mCherry in DA1 ORNs and HTT_{ex1}Q25-GFP in (**A**) mz0709+ ensheathing glia or (**B**) Alrm+ astrocytic glia. Scale bars = 5μm. (**C-D**) Quantification of (**C**) HTT_{ex1}Q91-mCherry aggregates and (**D**) seeded HTT_{ex1}Q25-GFP aggregates from flies shown in (**A-B**). Data are shown as mean±s.e.m.; ***p<0.001 by unpaired 2-tailed t-test; n≥14.

Supplemental Fig S5-1. Increased numbers of lysosomes associated with neuronal mHTT expression. (A-B) Maximum intensity projections of antennal lobes from 9-10 day-old flies expressing (**A**) HTT_{ex1}Q25- or (**B**) HTT_{ex1}Q91-GFP in Or83b+ ORNs. Brains were stained with Magic Red (MR) to label active cathepsins. Scale bars = 10μm. Fluorescence signal of HTT_{ex1}Q25 adjusted for easier visualization. (**C**) Quantification of MR+ surfaces and MR+ surfaces that co-localized with HTT-GFP signal from flies shown in (**A** and **B**). Data

are shown as mean±s.e.m.; ****p<0.0001 by unpaired 2-tailed t-test; n≥14. (**D-E**) Maximum intensity projections of antennal lobes from 15 day-old flies expressing (**D**) HTT_{ex1}Q25- or (**E**) HTT_{ex1}Q91-GFP in Or83b+ ORNs. Brains were stained with Lysotracker Red (LTR) to label low pH compartments. Fluorescence signal of HTT_{ex1}Q25 adjusted for easier visualization. Scale bars = 10μm. (**C**) Quantification of LTR+ surfaces and LTR+ surfaces that co-localized with HTT-GFP signal from flies shown in (**A** and **B**). Data are shown as mean±s.e.m.; ****p<0.0001 by unpaired 2-tailed t-test; n≥17.

Supplemental Fig S5-2. Knockdown of lysosomal acidification alters prion-like spreading of mHTT aggregates. (**A**) Maximum intensity projections of DA1 glomeruli from 8-9 day-old flies expressing HTT_{ex1}Q91-mCherry in DA1 ORNs and HTT_{ex1}Q25-GFP plus siRNAs targeting the indicated genes in repo+ glia. Negative controls expressed siRNAs targeting mCherry. Scale bars = 5μm. (**B-C**) Quantification of (**B**) mHTT or (**C**) mHTT+wtHTT aggregates from brains shown in (**A**). Data are shown as mean±s.e.m.; *p<0.05, ***p<0.005 by unpaired 2-tailed t-test; n≥16.

Supplemental Fig S5-3. GFP-LAMP1+ surfaces are associated with HTT surfaces. **A-B**) Magnified regions of confocal stacks showing antennal lobes from 21-22 day-old flies expressing (**A**) HTT_{ex1}Q25- or (**B**) HTT_{ex1}Q91-mCherry in Or83b+ ORNs and LAMP1 tagged at its luminal N-terminus with GFP (GFP-LAMP1) in glia. GFP-LAMP1+ or HTT+ surfaces identified by semi-automated image segmentation are shown to the right of each set of raw fluorescence images. GFP-LAMP1 surfaces isolated to highlight individual compartment associating with one or more HTT surfaces. Fluorescence signal of HTT_{ex1}Q25 adjusted for easier visualization. Scale bars as shown.

Supplemental Figure S7-1. Association of neuronal mHTT aggregates with Rab GTPases that label early, maturing, and late phagosomes. (A) qPCR analysis of *rab10*, *rab5*, and *rab7* expression in 8-11 day-old flies expressing GFP, HTT_{ex1}Q25-, or HTT_{ex1}Q91-GFP in Or83b+ ORNs. RNA was isolated from heads of uninjured flies or flies 3 hours after bilateral antennal and maxillary palp nerve injury. Data are shown as mean±s.e.m and normalized to the housekeeping gene *rpl32*. *p<0.05, **p<0.01, ***p<0.001 by one-way

74 ANOVA, asterisks and hashtags indicate statistical significance comparing -/+ injury or genotypes,
75 respectively; n=3. (**B-G**) Confocal stacks of the antennal lobe from 7 day-old flies expressing (**B, D, & F**)
76 HTT_{ex1}Q25- or (**C, E, & G**) HTT_{ex1}Q91-V5 in Or83b+ ORNs and endogenously-tagged (**B-C**) YRab10, (**D-E**)
77 YRab5, or (**F-G**) YRab7 in all cells. The brains were immunostained using YFP (*green*), V5 (*magenta*), and N-
78 Cadherin (*blue*) antibodies. YRab+ or HTT+ surfaces identified by semi-automated image segmentation are
79 shown to the right of each set of raw fluorescence images. Fluorescence signal of HTT_{ex1}Q25 adjusted for
80 easier visualization. Insets show magnified regions of interest. YRab surfaces isolated to highlight individual
81 compartment associating with one or more HTT surfaces. Scale bars = 10μm. (**H-I**) Quantification of (**H**)
82 YRab+ surfaces and (**I**) YRab+ surfaces that co-localized with HTT. Data are shown as mean±s.e.m.; *p<0.05,
83 **p<0.01, ****p<0.0001 by unpaired 2-tailed t-test; n≥16.

84

85 **Supplemental Figure S7-2**. **Glial Rab5 and Rab7 surfaces are associated with mHTT surfaces**. (**A-D**)
86 Confocal stacks of the antennal lobe from 16-19 day-old flies expressing (**A, C**) HTT_{ex1}Q25- or (**B, D**)
87 HTT_{ex1}Q91-V5 in Or83b+ ORNs and (**A-B**) YFP-Rab5, or (**C-D**) YFP-Rab7 in glia. Rab+ or HTT+ surfaces
88 identified by semi-automated image segmentation are shown to the right of each set of raw fluorescence
89 images. Fluorescence signal of HTT_{ex1}Q25 adjusted for easier visualization. Insets show magnified regions of
90 interest. YFP-Rab surfaces isolated to highlight individual compartment associating with one or more HTT
91 surfaces. Scale bars = 10μm.

92

93 **Supplementary Table 1. *Drosophila* lines used and source information.**

94

95 **Supplementary Table 2. Genotypes for figures and supplementary data figures.**

96

97 **Supplementary Table 3. Gene specific primers used for qPCR of adult *Drosophila* heads.**

98

99 **Supplementary Table 4. Statistical information for reported results.**

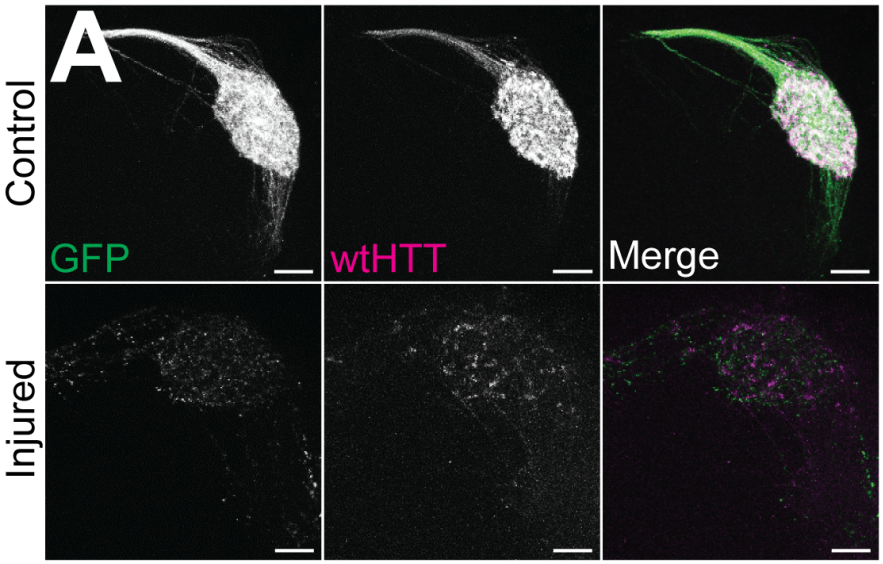
A
Control
Injured
GFP
wtHTT
Merge

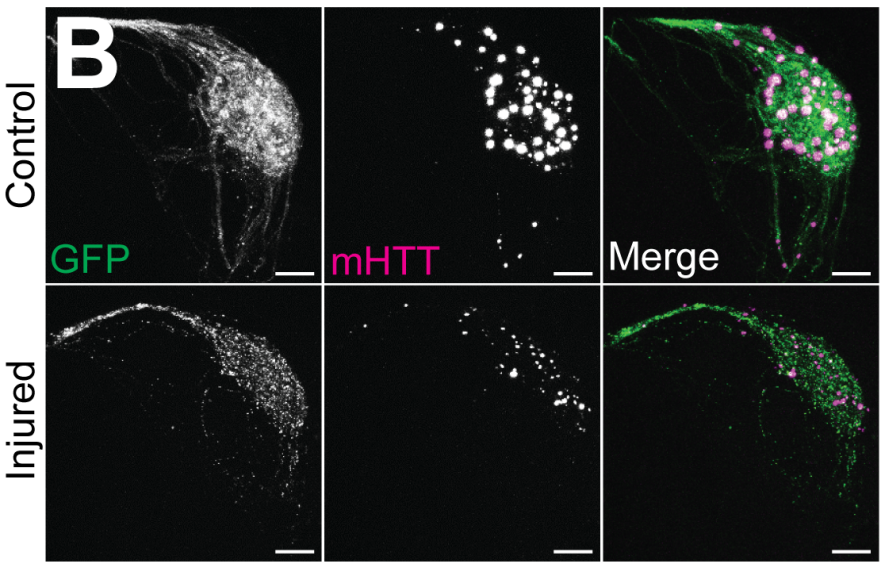
B
Control
Injured
GFP
mHTT
Merge

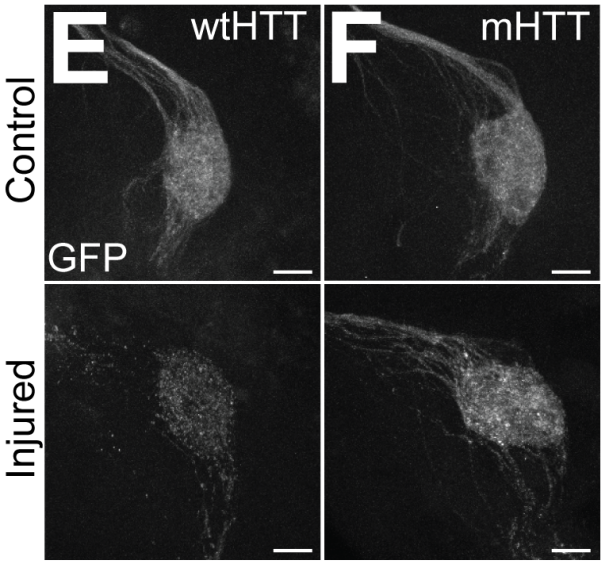
E
wtHTT
F
mHTT
Control
Injured
GFP

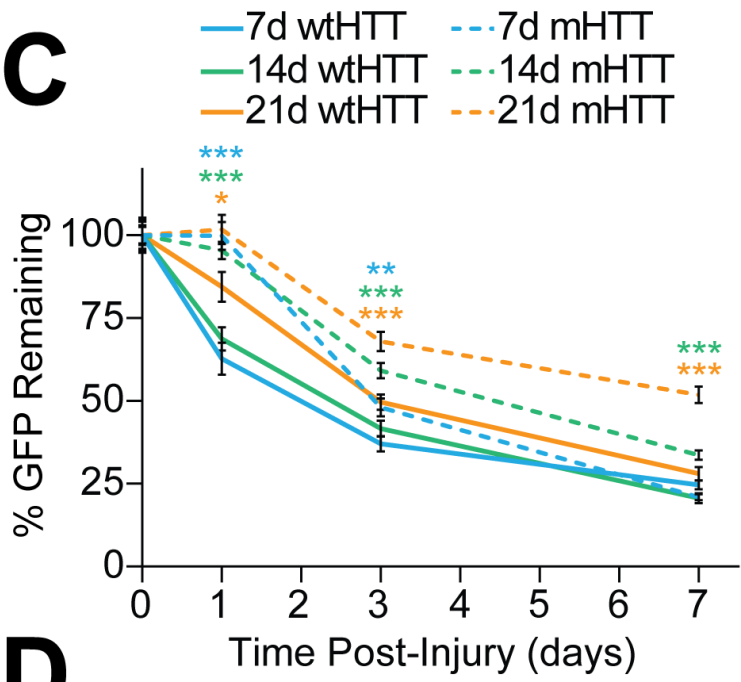
C
7d wtHTT
14d wtHTT
21d wtHTT
7d mHTT
14d mHTT
21d mHTT
% GFP Remaining
Time Post-Injury (days)

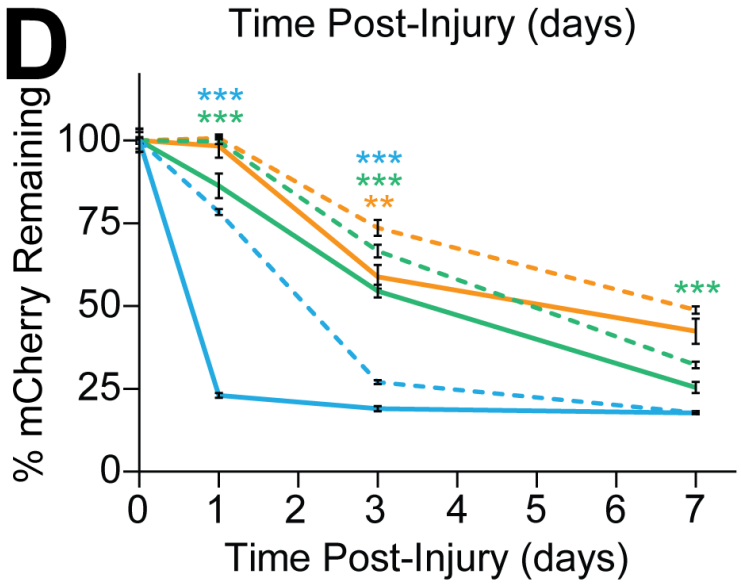
D
% mCherry Remaining
Time Post-Injury (days)

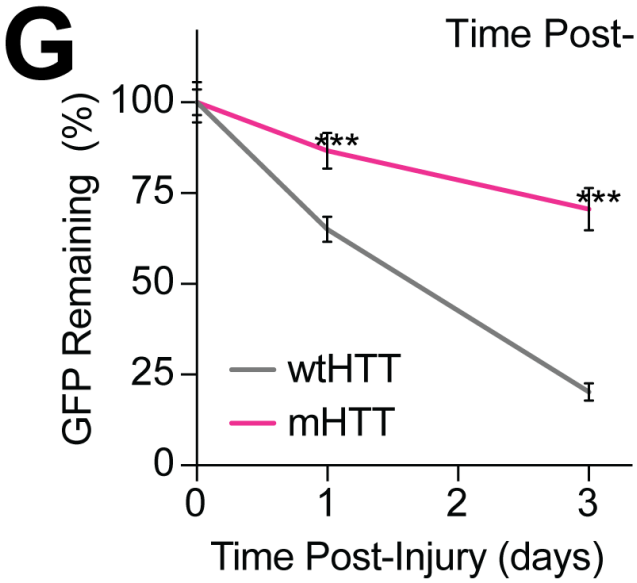
G
GFP Remaining (%)
wtHTT
mHTT
Time Post-Injury (days)

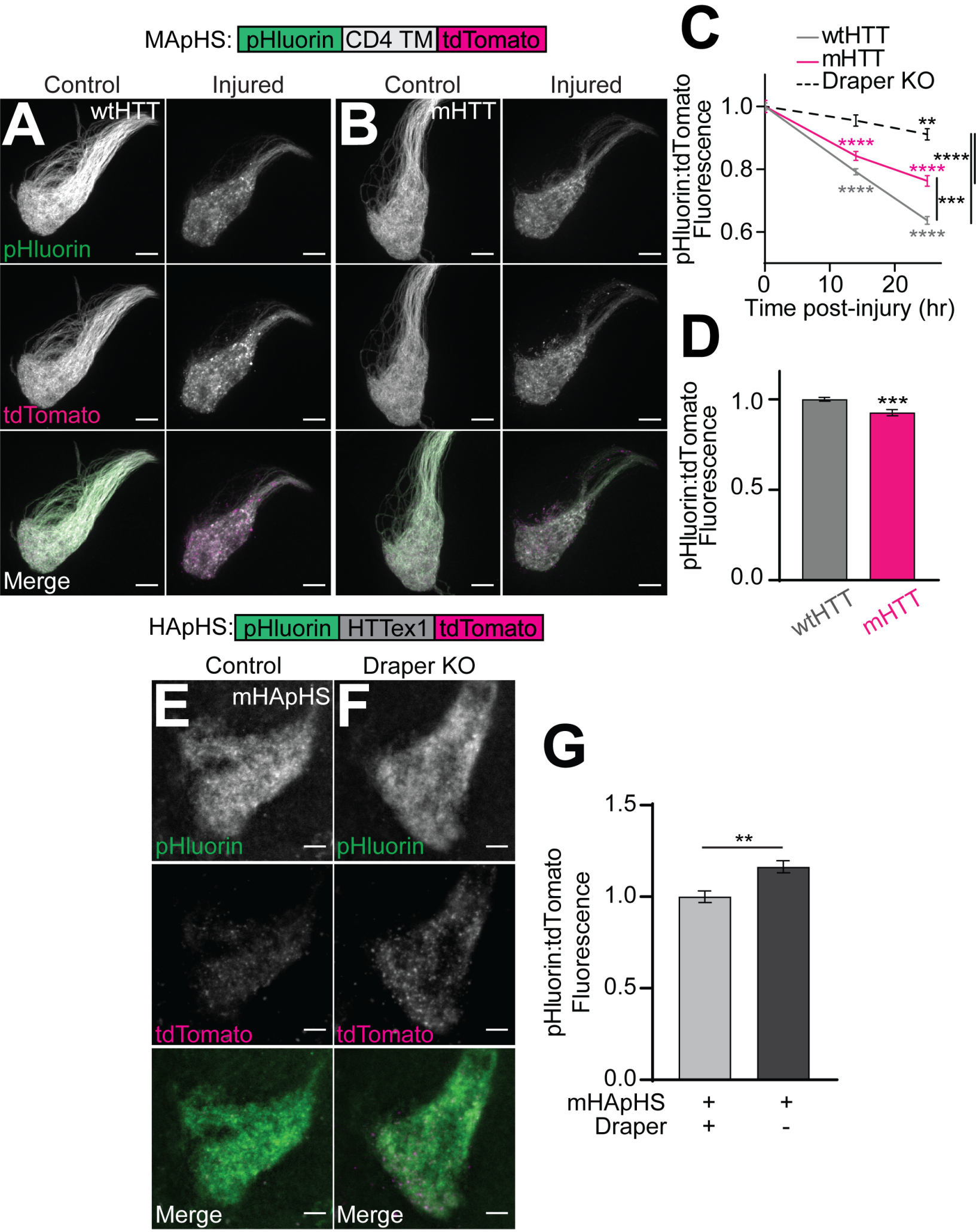
MApHS: pHluorin CD4 TM tdTomato
Control
Injured
Control
Injured
A
wtHTT
B
mHTT
pHluorin
tdTomato
Merge
C
wtHTT
mHTT
Draper KO
pHluorin:tdTomato Fluorescence
1.0
0.8
0.6
0
10
20
Time post-injury (hr)
**
****
***
D
pHluorin:tdTomato Fluorescence
1.0
0.5
0.0
***
wtHTT
mHTT
HApHS: pHluorin HTTex1 tdTomato
Control
Draper KO
E
mHApHS
F
pHluorin
tdTomato
Merge
G
pHluorin:tdTomato Fluorescence
1.5
1.0
0.5
0.0
**
mHApHS + +
Draper + -

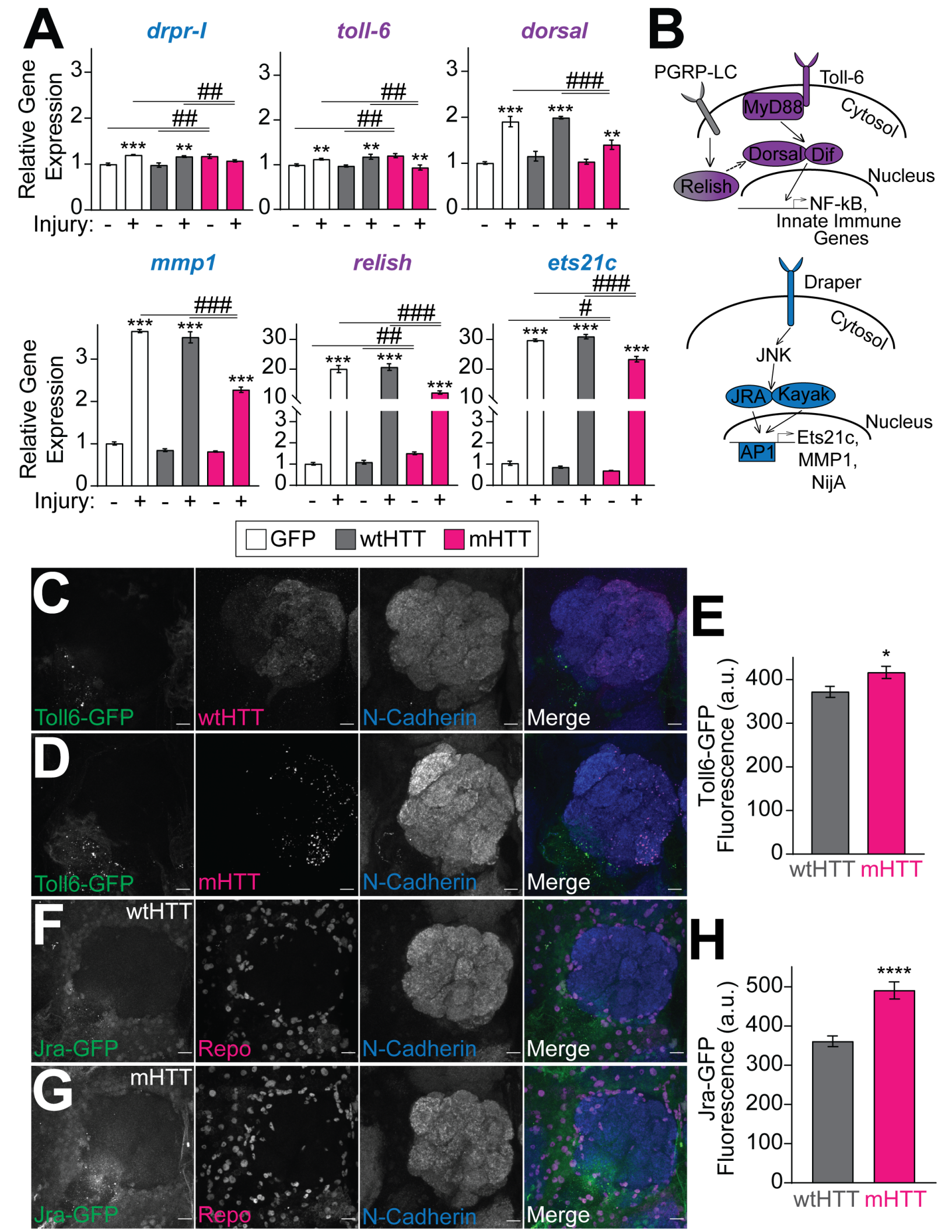
A
drpr-l
toll-6
dorsal
mmp1
relish
ets21c
Relative Gene Expression
Injury: - + - + - +
GFP
wtHTT
mHTT
B
PGRP-LC
Toll-6
MyD88
Cytosol
Dorsal
Dif
Relish
Nucleus
NF-kB, Innate Immune Genes
Draper
Cytosol
JNK
JRA
Kayak
Nucleus
AP1
Ets21c, MMP1, NijA
C
Toll6-GFP
wtHTT
N-Cadherin
Merge
D
Toll6-GFP
mHTT
N-Cadherin
Merge
E
Toll6-GFP Fluorescence (a.u.)
wtHTT
mHTT
F
wtHTT
Jra-GFP
Repo
N-Cadherin
Merge
G
mHTT
Jra-GFP
Repo
N-Cadherin
Merge
H
Jra-GFP Fluorescence (a.u.)
wtHTT
mHTT

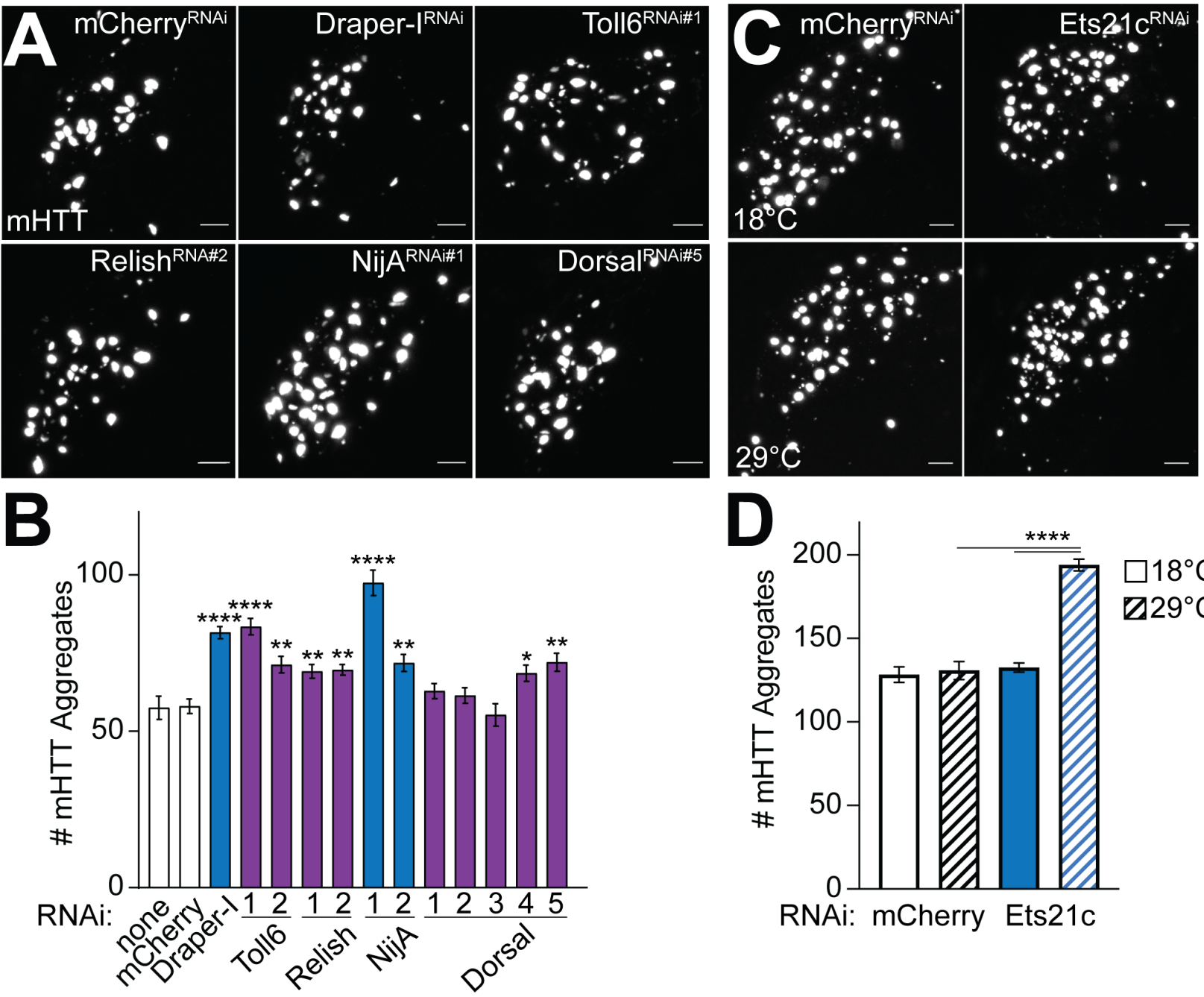
A
mCherryRNAi
Draper-IRNAi
Toll6RNAi#1
mHTT
RelishRNA#2
NijARNAi#1
DorsalRNAi#5
B
mHTT Aggregates
100
50
0
****
****
**
**
**
****
**
*
**
RNAi:
none
mCherry
Draper-I
1 2
Toll6
1 2
Relish
1 2
NijA
1 2 3 4 5
Dorsal
C
mCherryRNAi
Ets21cRNAi
18°C
29°C
D
mHTT Aggregates
200
150
100
50
0
****
18°C
29°C
RNAi: mCherry Ets21c

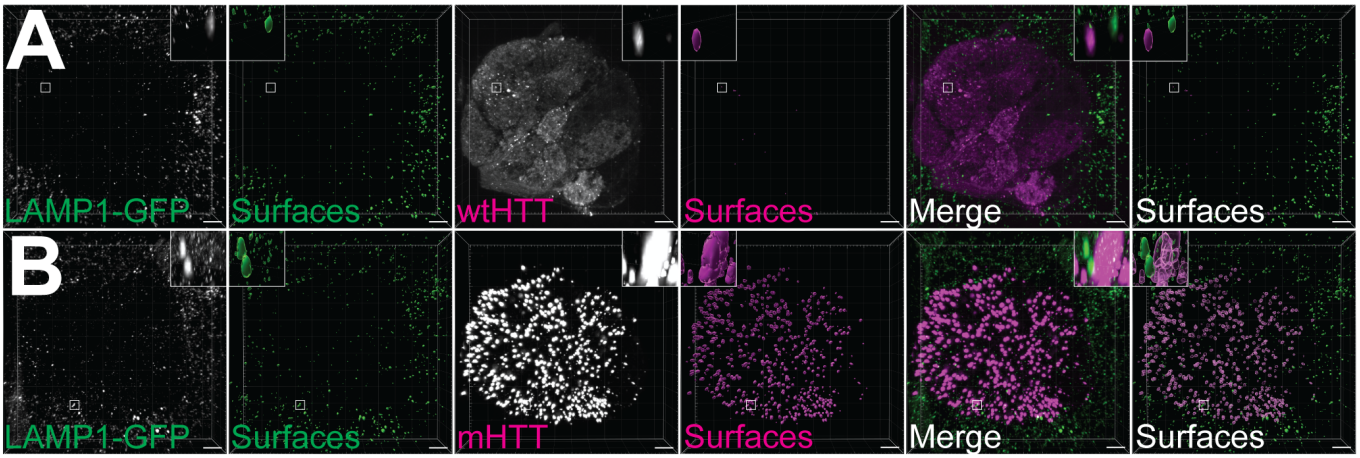
A
LAMP1-GFP
Surfaces
wtHTT
Surfaces
Merge
Surfaces
B
LAMP1-GFP
Surfaces
mHTT
Surfaces
Merge
Surfaces

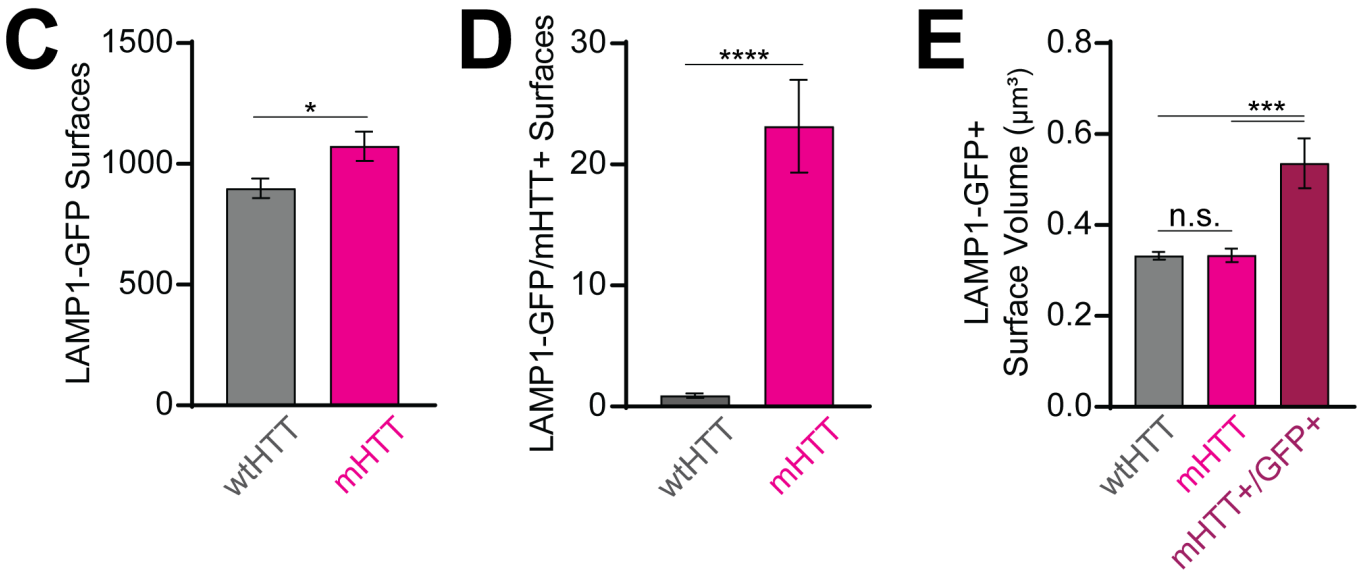
C
LAMP1-GFP Surfaces
1500
1000
500
0
*
wtHTT
mHTT
D
LAMP1-GFP/mHTT+ Surfaces
30
20
10
0
****
wtHTT
mHTT
E
LAMP1-GFP+
Surface Volume (µm³)
0.8
0.6
0.4
0.2
0.0
***
n.s.
wtHTT
mHTT
mHTT+/GFP+

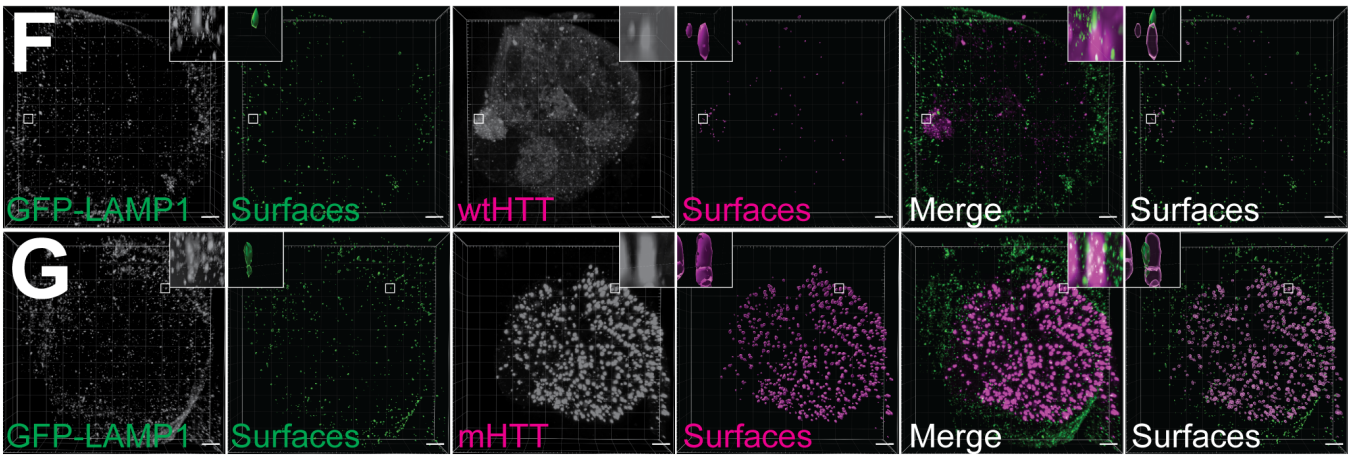
F
GFP-LAMP1
Surfaces
wtHTT
Surfaces
Merge
Surfaces
G
GFP-LAMP1
Surfaces
mHTT
Surfaces
Merge
Surfaces

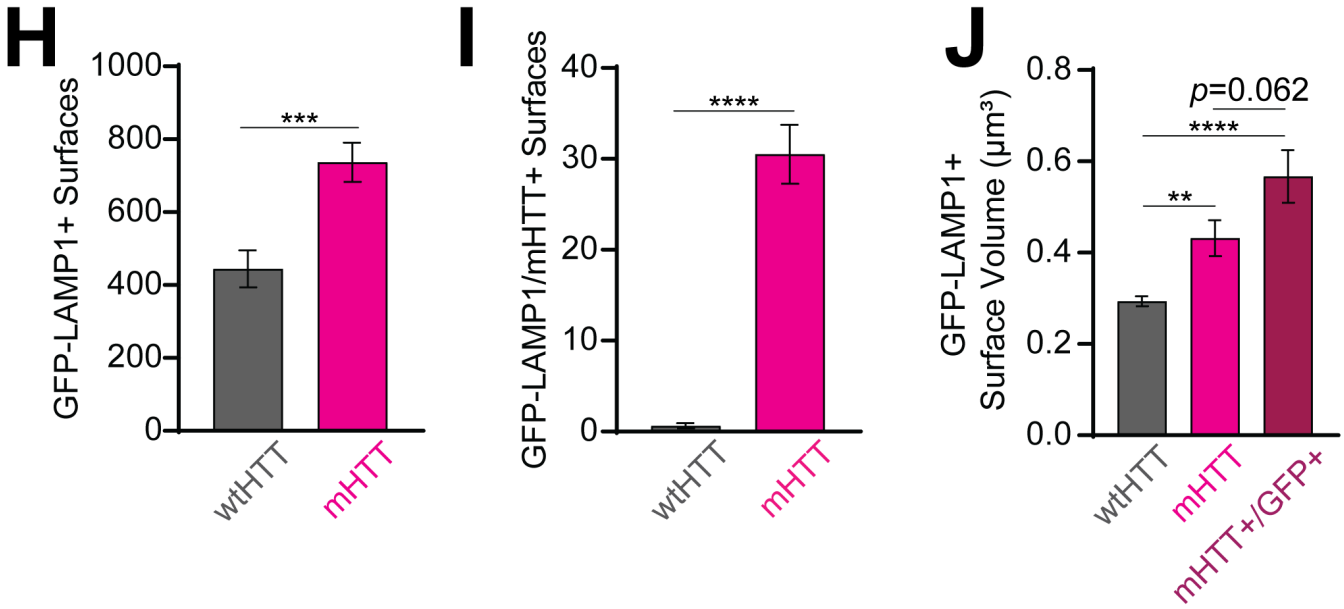
H
GFP-LAMP1+ Surfaces
1000
800
600
400
200
0
***
wtHTT
mHTT
I
GFP-LAMP1/mHTT+ Surfaces
40
30
20
10
0
****
wtHTT
mHTT
J
GFP-LAMP1+
Surface Volume (µm³)
0.8
0.6
0.4
0.2
0.0
p=0.062
****
**
wtHTT
mHTT
mHTT+/GFP+

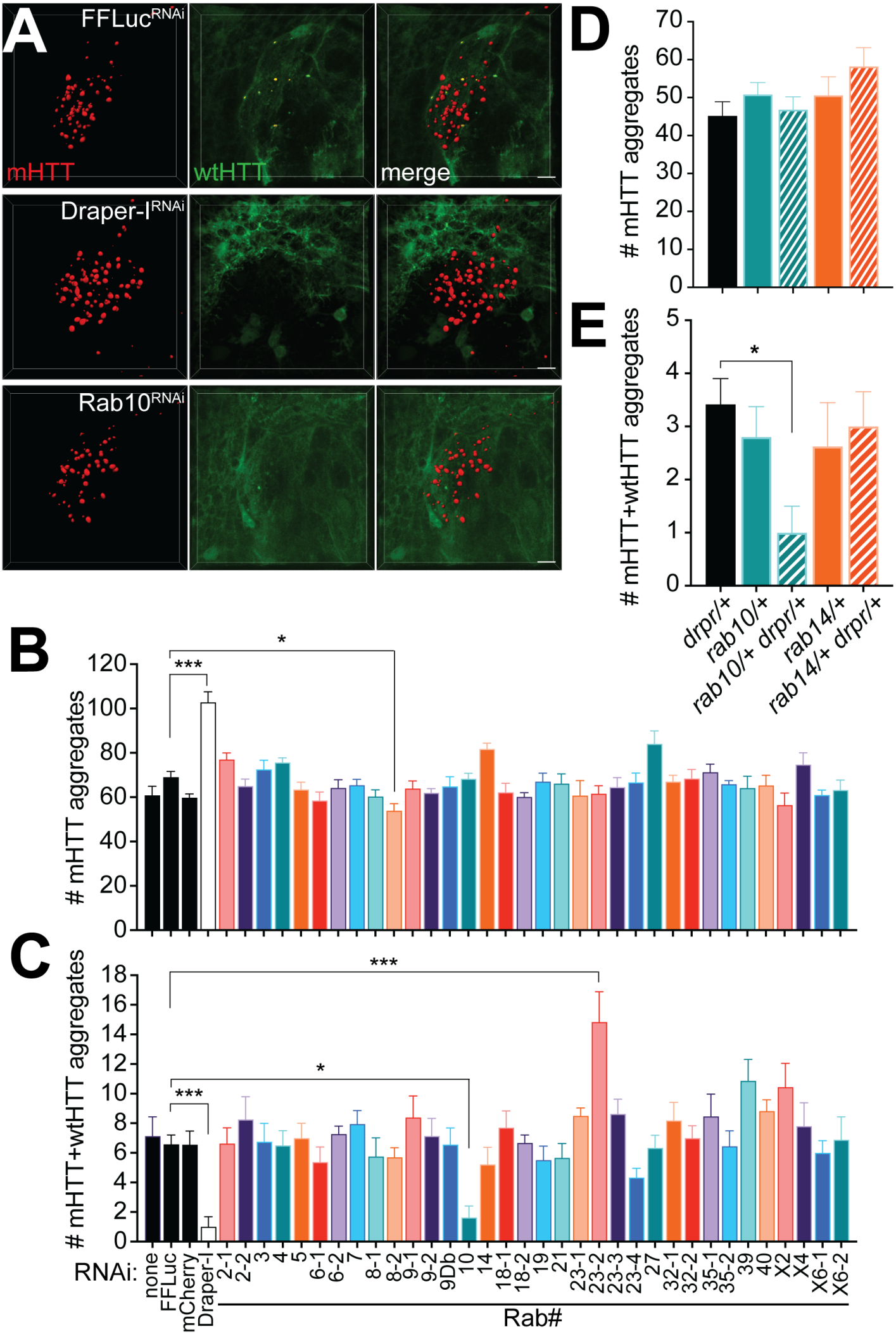
A
FFLucRNAi
mHTT
wtHTT
merge
Draper-IRNAi
Rab10RNAi
D
mHTT aggregates
E
mHTT+wtHTT aggregates
drpr/+
rab10/+
rab10/+ drpr/+
rab14/+
rab14/+ drpr/+
B
mHTT aggregates
C
mHTT+wtHTT aggregates
RNAi:
none
FFLuc
mCherry
Draper-I
2-1
2-2
3
4
5
6-1
6-2
7
8-1
8-2
9-1
9-2
9Db
10
14
18-1
18-2
19
21
23-1
23-2
23-3
23-4
27
32-1
32-2
35-1
35-2
39
40
X2
X4
X6-1
X6-2
Rab#

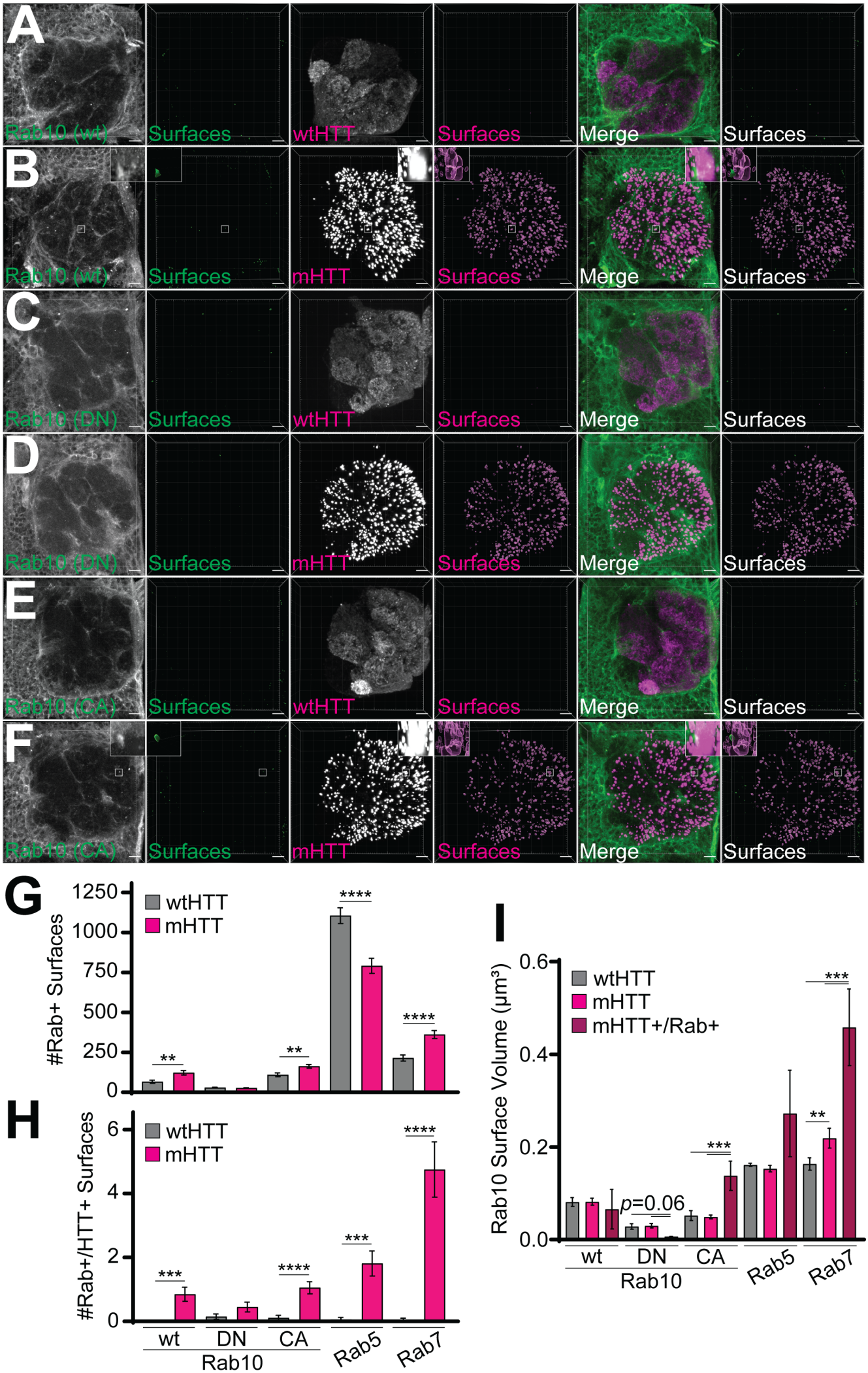
A
Rab10 (wt)
Surfaces
wtHTT
Surfaces
Merge
Surfaces
B
Rab10 (wt)
Surfaces
mHTT
Surfaces
Merge
Surfaces
C
Rab10 (DN)
Surfaces
wtHTT
Surfaces
Merge
Surfaces
D
Rab10 (DN)
Surfaces
mHTT
Surfaces
Merge
Surfaces
E
Rab10 (CA)
Surfaces
wtHTT
Surfaces
Merge
Surfaces
F
Rab10 (CA)
Surfaces
mHTT
Surfaces
Merge
Surfaces
G
#Rab+ Surfaces
1250
1000
750
500
250
0
wtHTT
mHTT
**
**
****
****
H
#Rab+/HTT+ Surfaces
6
4
2
0
wtHTT
mHTT
***
****
***
****
wt
DN
CA
Rab10
Rab5
Rab7
I
Rab10 Surface Volume (µm³)
0.6
0.4
0.2
0.0
wtHTT
mHTT
mHTT+/Rab+
p=0.06
***
***
**
wt
DN
CA
Rab10
Rab5
Rab7